

Supporting Information for

Self-assembly of a trigonal bipyramidal architecture with stabilisation of iron in three spin states

Lauren L. K. Taylor,^a Iñigo J. Vitorica-Yrezabal,^a Ivana Borilović,^{a,b} Floriana Tuna,^{a,b*}

Imogen A. Riddell^{*a}

^a Department of Chemistry, University of Manchester, Oxford Road, Manchester, M13 9PL
(UK)

^b Photon Science Institute, University of Manchester, Oxford Road, Manchester, M13 9PL
(UK)

*Email: imogen.riddell@manchester.ac.uk; floriana.tuna@manchester.ac.uk

Table of Contents

S1	Synthesis and Characterization	S2
S1.1	General Experimental Details	S2
S1.2	Ligand Synthesis	S3
S1.3	Iron Self-Assembly Reactions	S8
S2	X-Ray Crystallography	S16
S3	Bond Valence Sum (BVS) Analysis	S22
S3.1	Complex 1	S23
S3.2	Complex 2	S24
S3.3	Complex 3	S26
S4	UV-Vis Spectroscopy	S28
S5	SQUID Magnetometry	S29
S6	EPR Spectroscopy	S37
S7	References	S38

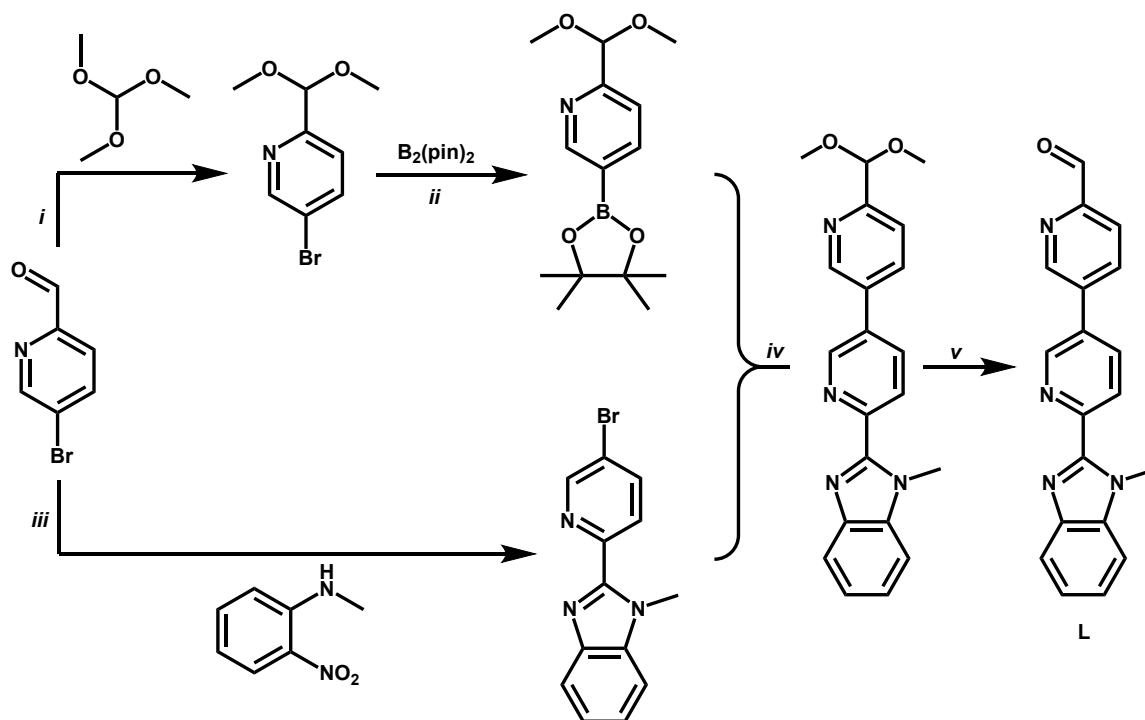
S1 Synthesis and Characterization

S1.1 General Experimental Details

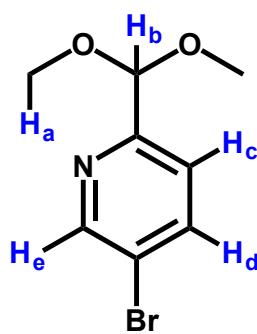
Unless stated otherwise, all chemicals were supplied from Sigma-Aldrich, Fluorochem, Fisher Scientific, Alfa Aesar or Scientific Laboratory Supplies Ltd and used without further purification. Deuterated NMR solvents were supplied from Sigma-Aldrich and NMR spectra were recorded on a B500 Bruker Advance II+ 500 MHz spectrometer. Chemical shifts are reported in parts per million (ppm). Coupling constants (J) are reported in hertz (Hz). Standard abbreviations indicating multiplicity were used as follows: s = singlet, d = doublet, t = triplet, dd = doublet of doublets, m = multiplet. ^1H and ^{13}C assignments were made using 2D NMR methods (COSY, NOESY, HSQC, HMBC). High resolution mass spectra were obtained using a Thermo Orbitrap Exactive Plus Extended Mass Range mass spectrometer. Elemental analyses were performed by the microanalytical services of The University of Manchester with a CFlash 2000 elemental analyser for the analyses of carbon, hydrogen and nitrogen. The DOSY experiment was performed using a stimulated echo sequence with bipolar gradients (Bruker standard sequence ledbpgp2s). The experiment was performed using 10 gradient steps with a minimum nominal gradient of 75 G/cm and a maximum 300 G/cm, incremented in steps of gradient squared. Smoothed-square gradients with a duration of 0.5 ms were used. Gradient recovery delay was 20 μs and diffusion time was 4 ms. The dataset was processed using GNAT¹ and hydrodynamic radii were calculated using the Stokes-Einstein-Gierer-Wirtz approach.^{2,3} Experiments were acquired at 298 K using a Bruker 500 NEO NMR spectrometer equipped with 5 mm diffusion probe.

S1.2 Ligand Synthesis

Scheme S1: Synthesis of asymmetric ligand **L** via a convergent synthesis strategy starting from 5-bromo-2-pyridinecarboxaldehyde. i) *p*-TsOH, ii) Pd(dppf)Cl₂.CH₂Cl₂, KOAc, iii) Na₂S₂O₅, iv) Pd(PPh₃)₄, Na₂CO₃, v) HCl (2 M).



5-Bromo-2-(dimethoxymethyl)pyridine: 5-Bromo-2-pyridinecarboxaldehyde (1.6 g, 8.6



mmol) and *p*-toluenesulfonic acid monohydrate (34 mg, 0.18 mmol) were dissolved in dry methanol (32 mL). Trimethyl orthoformate (4.7 mL, 43.0 mmol) was added and the brown solution was refluxed under N₂ (100°C, 24 hr). The solvent was removed *in vacuo* giving an orange oil that was dissolved in dichloromethane and neutralised with NaHCO₃. The product was extracted with dichloromethane (3 x 20 mL) and dried over MgSO₄. After filtering, the solvent was removed under reduced

pressure to give the product as a brown oil (1.56 g, 6.75 mmol, 79%). ¹H (500 MHz, 298 K, CDCl₃): δ = 8.60 (d, 1H, *J* = 2.30 Hz, H_e), 7.78 (dd, 1H, *J* = 2.33, 8.38 Hz, H_a), 7.39 (d, 1H, *J* = 8.35 Hz, H_c), 5.27 (s, 1H, H_b), 3.32 (s, 6H, H_a). ¹³C (125.8 MHz, 300 K, CDCl₃): 155.9, 150.3, 139.3, 122.7, 120.6, 103.3, 53.6. [Accurate mass]: expected = 230.9895, found = 231.9960 [M + H]⁺.

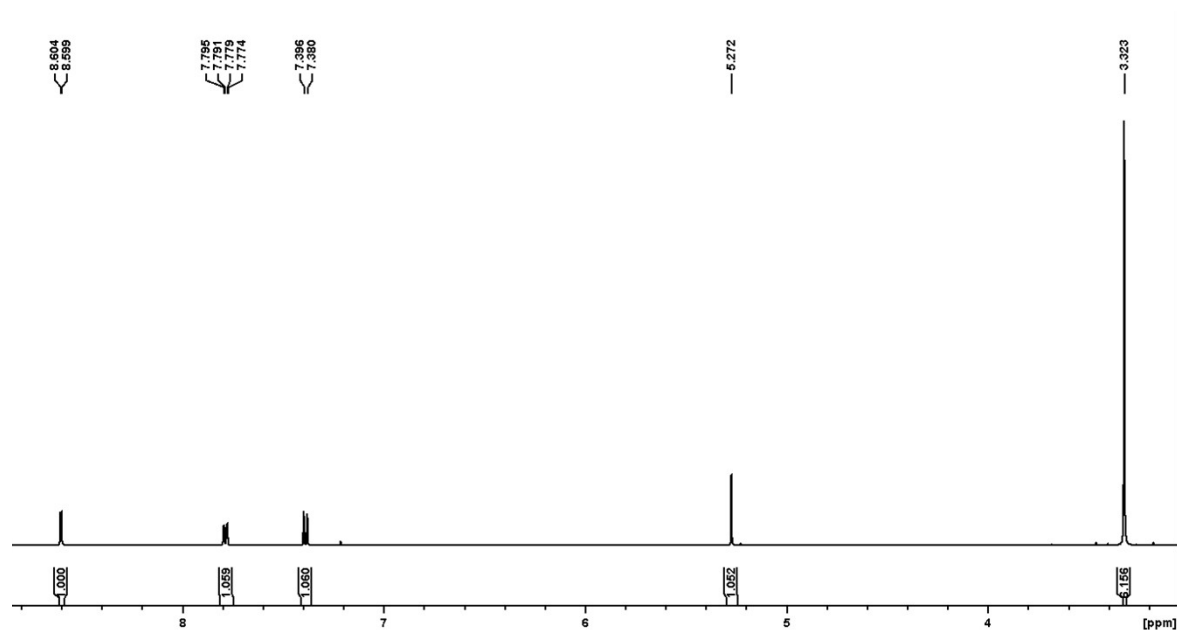
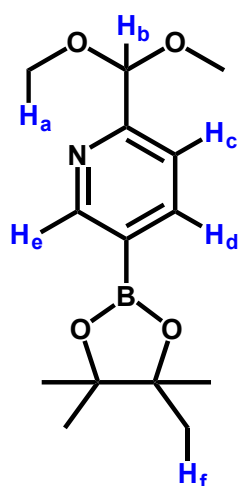


Figure S1: ^1H NMR (500 MHz, CDCl_3 , 298 K) spectrum of protected aldehyde 5-bromo-2-(dimethoxymethyl)pyridine.

2-(Dimethoxymethyl)-5-(4,4,5,5-tetramethyl-1,3,2-dioxaborolan-2-yl)pyridine:



5-Bromo-2-(dimethoxymethyl)pyridine (0.84 g, 3.64 mmol), bis(pinacolato)diboron (1.1 g, 4.37 mmol), potassium acetate (1.1 g, 10.9 mmol) and $\text{Pd}(\text{dppf})\text{Cl}_2 \cdot \text{CH}_2\text{Cl}_2$ (0.15 g, 0.18 mmol) were dissolved in DMF (22 mL) and the orange solution was heated under N_2 (50°C, 24 hr). The solvent was removed *in vacuo* and the resulting brown solid was dissolved in diisopropyl ether. The suspended brown solid was filtered off, and the solvent was removed *in vacuo* to give a green oil that was then dissolved in hexane. The insoluble material was filtered off and the solvent was removed to yield the final product as a green oil (0.65 g, 2.34 mmol, 64%). ^1H (500 MHz, 298 K, CDCl_3): δ = 8.87 (s, 1H, H_e), 8.03 (d, 1H, J = 7.61 Hz, H_d), 7.47 (d, 1H, J = 7.69 Hz, H_c), 5.33 (s, 1H, H_b), 3.32 (s, 6H, H_a), 1.28 (s, 12H, H_f).

^{13}C (125.7 MHz, 300 K, CDCl_3): 159.3, 154.9, 143.1, 135.1, 120.6, 103.8, 84.3, 53.5, 24.9, 24.8. [Accurate mass]: expected = 279.1642, found = 279.1743 $[\text{M}]^+$, 280.1705 $[\text{M} + \text{H}]^+$.

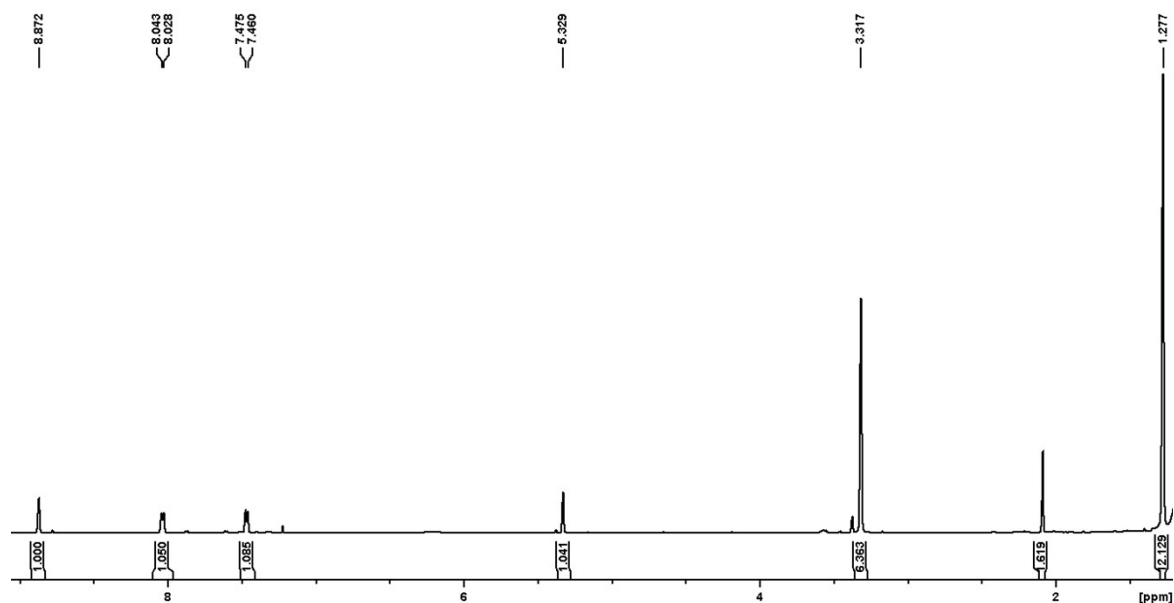
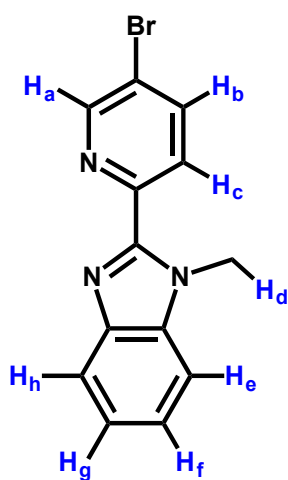


Figure S2: ^1H NMR (500 MHz, CDCl_3 , 298 K) spectrum of 2-(dimethoxymethyl)-5-(4,4,5,5-tetramethyl-1,3,2-dioxaborolan-2-yl)pyridine.

2-(5-Bromopyridin-2-yl)-1-methyl-1H-benzo[d]imidazole:



5-Bromo-2-pyridinecarboxaldehyde (2 g, 10.7 mmol) and *N*-methyl-2-nitroaniline (1.6 g, 10.7 mmol) were dissolved in a 4:1 mixture of DMF:H₂O (72 mL). The resulting orange solution was degassed by three vacuum/N₂ fill cycles before Na₂S₂O₅ (6.1 g, 32 mmol) was added. The solution was stirred under reflux (24 hr) which turned the solution green then eventually gave a cloudy yellow solution that was added to an ethyl acetate/water mixture. The aqueous layer was washed with ethyl acetate (3 x 30 mL) and the organic layers were combined and dried over MgSO₄. Filtration and removal of the solvent *in vacuo* yielded a yellow crystalline solid (2.4 g, 8.5 mmol, 79%). Crystals suitable for X-ray diffraction were obtained through slow evaporation of CHCl₃. ^1H (500 MHz, 298 K, CDCl_3): δ = 8.68 (s, 1H, *H_a*), 8.25 (d, 1H, *J* = 8.50 Hz, *H_c*), 7.90 (d, 1H, *J* = 8.50 Hz, *H_b*), 7.75 (d, 1H, *J* = 7.85 Hz, *H_h*), 7.37 (d, 1H, *J* = 7.90 Hz, *H_e*), 7.29 (t, 1H, *J* = 7.49 Hz, *H_g*), 7.25 (t, 1H, *J* = 7.45 Hz, *H_f*), 4.19 (s, 3H, *H_d*). ^{13}C (126 MHz, 300 K, CDCl_3): 149.65, 149.27, 149.06, 142.51, 139.52, 137.35, 125.85, 123.62, 122.81, 121.25, 120.09, 109.98, 30.91. [Accurate mass]: expected = 287.0058, found = 288.0121 [*M* + *H*]⁺.

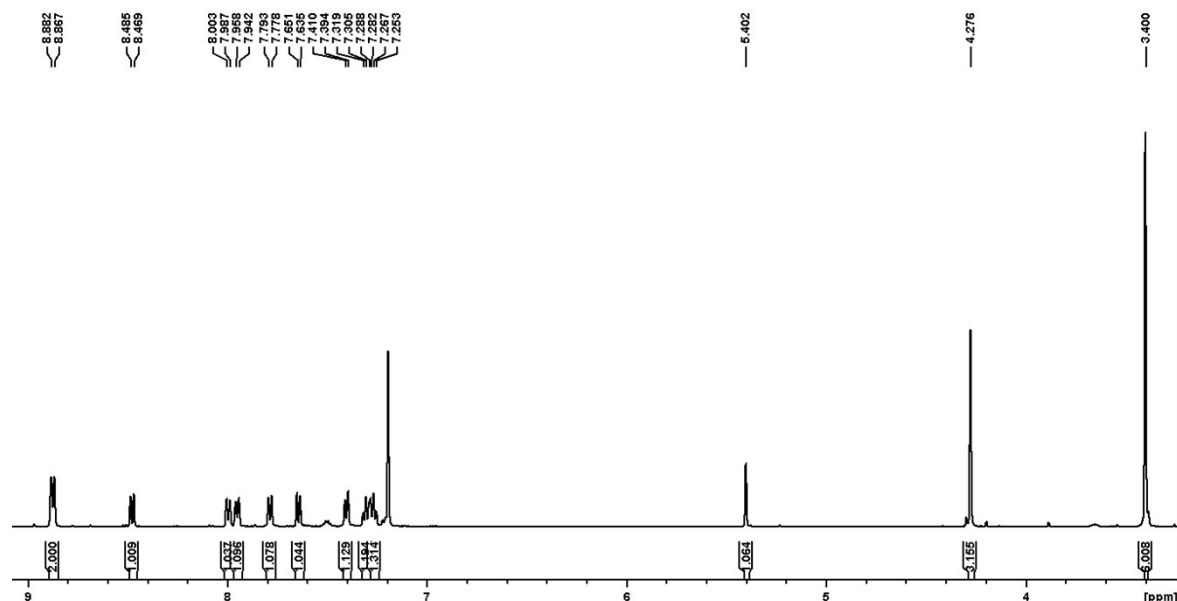
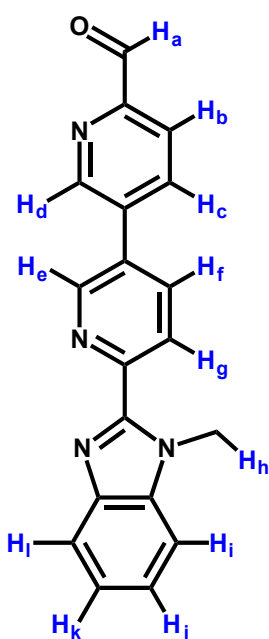


Figure S4: ^1H NMR (500 MHz, CD_3CN , 298 K) spectrum of the protected ligand.

Target Ligand, L: Protected ligand, **L'** (99 mg, 0.27 mmol) was dissolved in THF (1.5 mL)



and HCl (2 M, 2.9 mL) was added. The yellow solution was sealed under N_2 and heated (40°C , 22 hr) before being neutralised by the addition of saturated NaHCO_3 , resulting in the formation of a white precipitate. The white solid was dissolved in a 3:1 mixture of CHCl_3 :2-propanol and the aqueous layer was washed with CHCl_3 (3 x 5 mL) before being dried over MgSO_4 and filtered to give a yellow solid (62 mg, 0.20 mmol, 73%). ^1H (500 MHz, 298 K, CD_3CN): δ = 10.01 (s, 1H, H_a), 9.11 (s, 1H, H_d), 9.02 (s, 1H, H_e), 8.43 (d, 1H, J = 8.26 Hz, H_f), 8.25 (d, 1H, J = 7.93 Hz, H_c), 8.21 (d, 1H, J = 8.34 Hz, H_g), 8.00 (d, 1H, J = 8.11 Hz, H_b), 7.67 (d, 1H, J = 7.94 Hz, H_l), 7.50 (d, 1H, J = 8.11 Hz, H_i), 7.30 (t, 1H, J = 7.51 Hz, H_j), 7.24 (t, 1H, J = 7.51 Hz, H_k), 4.24 (s, 3H, H_h). ^{13}C (126 MHz, 300 K, CDCl_3): 32.97, 110.08, 120.24, 122.02, 122.97, 123.79, 124.91, 131.97, 135.34, 137.09, 137.49, 142.67, 147.05, 148.49, 149.40, 151.18, 152.29, 192.84. [Accurate mass]: expected = 314.1168, found = 315.1228 $[\text{M} + \text{H}]^+$.

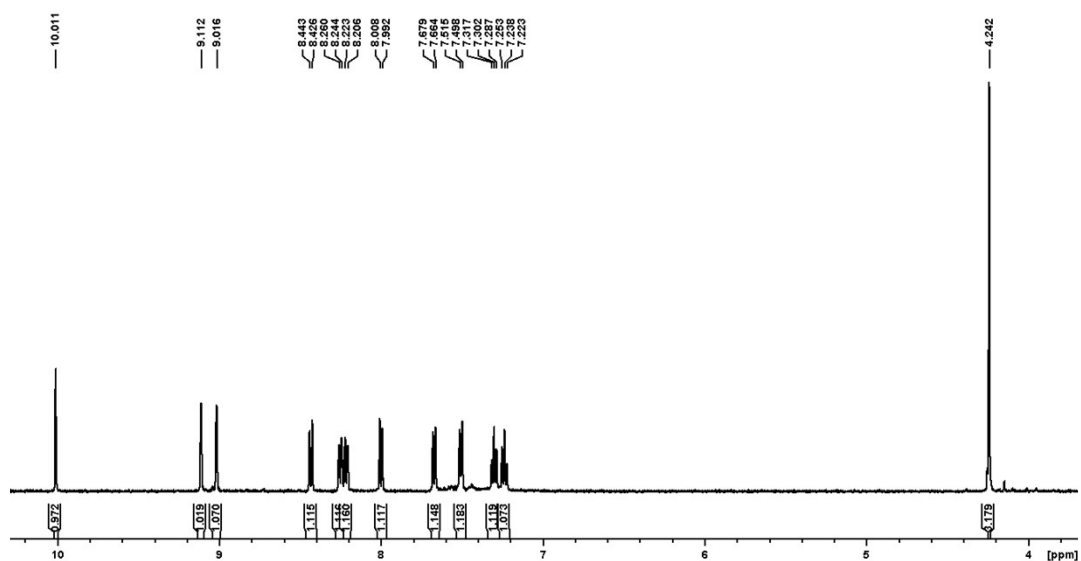
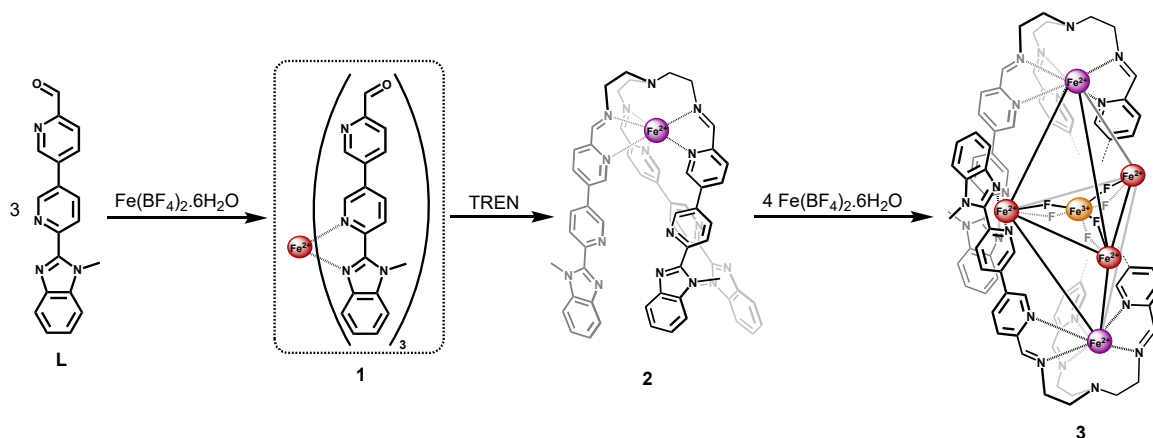


Figure S5: ^1H NMR (500 MHz, CD_3CN , 298 K) spectrum of the final ligand, **L**, following deprotection with HCl.

S1.3 Iron Self-Assembly Reactions

Scheme S2: Stepwise formation of **3** proceeds through iron(II) intermediates **1** and **2**.



S1.3.1 Complex 1; $[\text{Fe}^{\text{II}}\text{L}_3](\text{BF}_4)_2$

Ligand **L** (10 mg, 31.81 μmol , 3 equiv) and $\text{Fe}(\text{BF}_4)_2 \cdot 6\text{H}_2\text{O}$ (3.58 mg, 10.60 μmol , 1 equiv) were dissolved in deuterated acetonitrile (0.5 mL) and the resulting red solution was added to a J-Young NMR tube. The tube was sealed, and the solution was degassed by three vacuum/ N_2 fill cycles before being heated (50°C, 24 hr). Diethyl ether was added to the red solution, causing precipitation of the product which was washed with chloroform to give a red solid (4.3 mg, 3.94 μmol , 37%) [Accurate mass, m/z]: $\{\text{FeL}_3\}^{2+} = 499.1435$, $\{\text{FeL}_3\}(\text{BF}_4)^+ = 1085.2915$. Elemental analysis (%) calculated for $\text{C}_{63}\text{H}_{54}\text{B}_2\text{F}_8\text{FeN}_{16} \cdot 3.65 \text{CHCl}_3$: C 53.69, H 3.93, N 12.39; found: C 53.69, H 3.93, N 12.11.

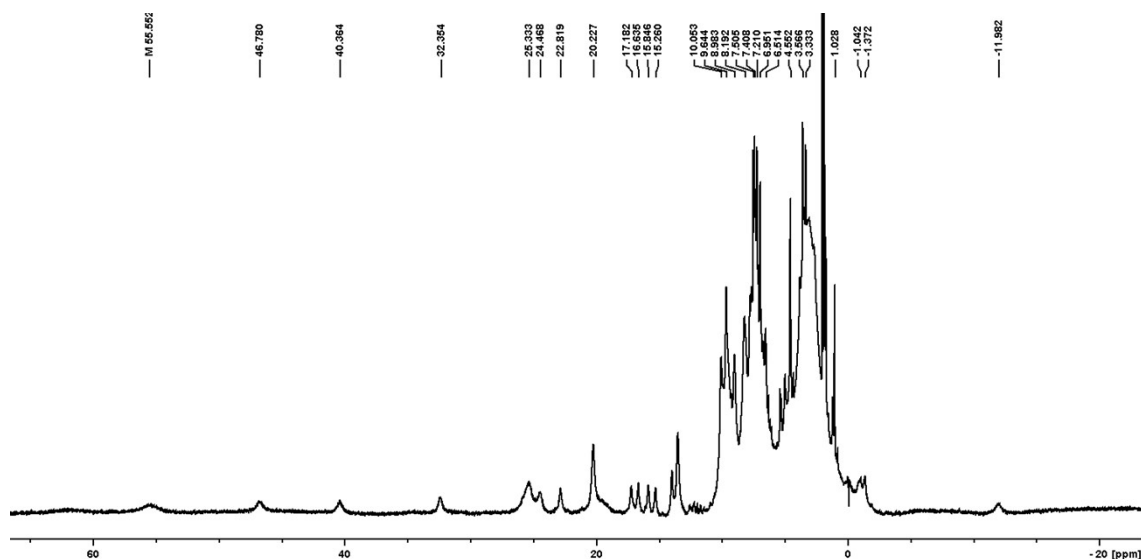


Figure S6: ^1H NMR (500 MHz, CD_3CN , 298 K) spectrum of the dynamic mixture containing complex **1**.

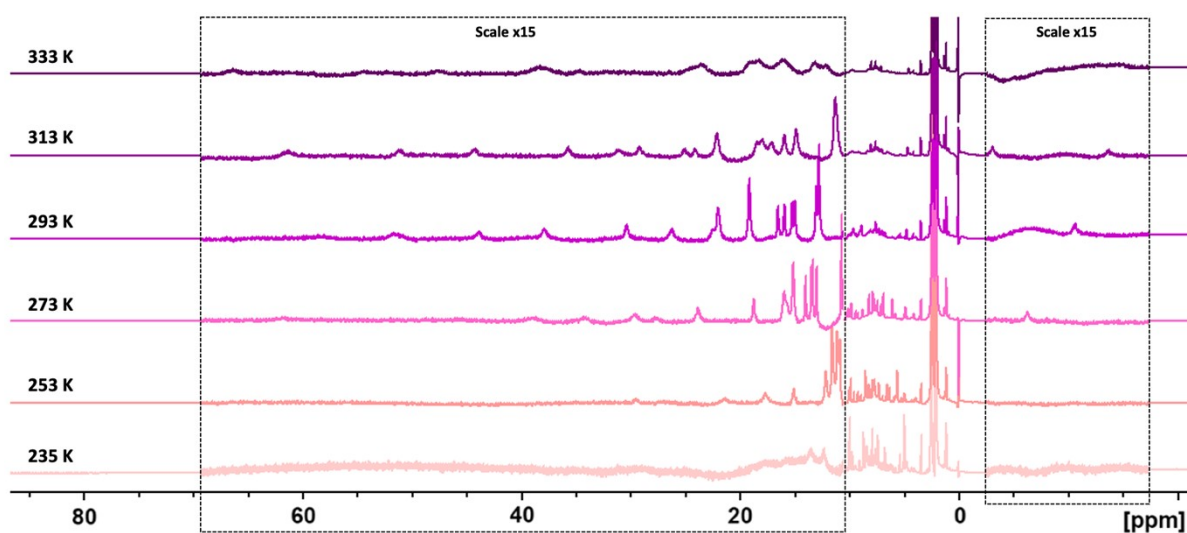


Figure S7: ^1H NMR (500 MHz, CD_3CN) spectra of dynamic mixture containing complex **1** recorded at temperatures from 235 K (bottom) to 333 K (top) in five steps of 20 K. At room temperature, the ^1H NMR spectrum of complex **1** contains peaks between 20 – 60 ppm indicating a significant fraction of the sample exists as HS Fe(II).

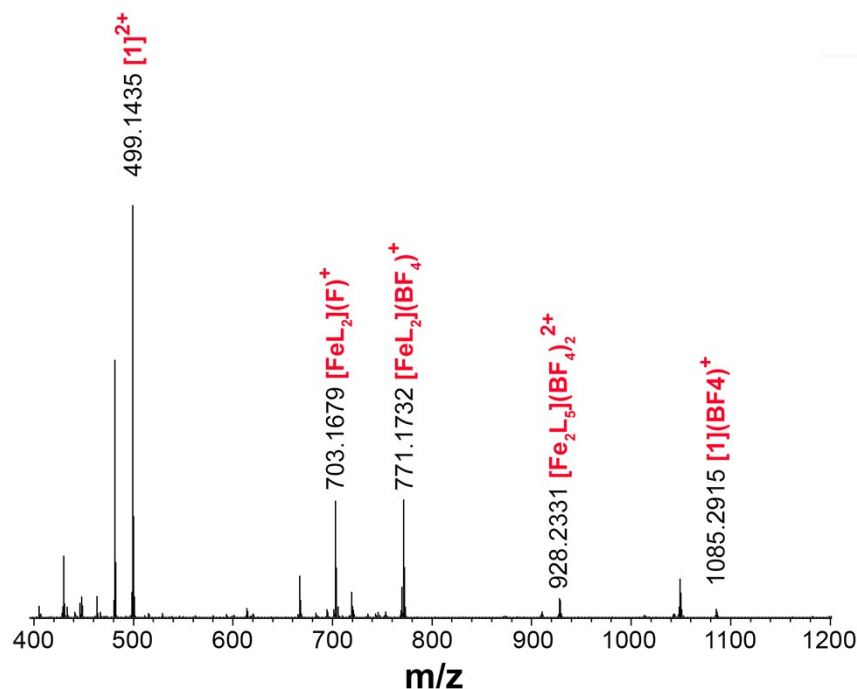
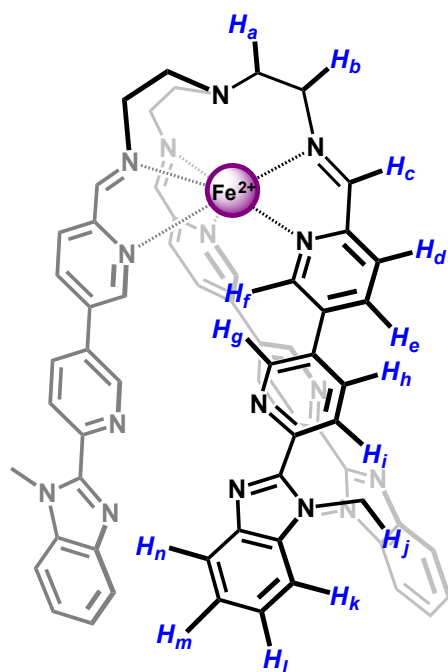


Figure S8: High-resolution mass spectrum for an acetonitrile solution of complex **1**, annotating additional isotopic patterns that were also present.

S1.3.2 Complex 2; $[\text{FeL}_3\text{T}](\text{BF}_4)_2$

To a solution of complex **1** in a J-Young NMR tube, *tris*(2-aminoethyl)amine (TREN, T) (1.94



μL , 12.94 μmol , 1 equiv) was added. The tube was sealed, and the resulting blue solution was degassed by three vacuum/ N_2 fill cycles before being heated (50°C, 24 hr). Diethyl ether was added to the resulting purple solution, causing precipitation of the product which was washed with chloroform to give a purple solid. ^1H (500 MHz, 298 K, CD_3CN): δ = 9.28 (s, 1H, H_c), 8.71 (s, 1H, H_f), 8.46 (broad s, 1H, H_g), 8.38 (broad s, 1H, H_h), 8.30 (d, 1H, J = 7.86 Hz, H_e), 7.86 (d, 1H, J = 7.79 Hz, H_d), 7.61 (d, 1H, J = 7.45 Hz, H_k), 7.45 (d, 2H, J = 7.99 Hz, H_n/H_i), 7.27 (t, 1H, J = 7.47 Hz, H_m), 7.20 (t, 1H, J = 7.49 Hz, H_l), 4.12 (s, 3H, H_j), 3.73 (m, 1H, H_b), 3.58 (m, 1H, H_a), 3.19 (broad t, 1H, H_b), 3.09 (broad t, 1H, H_a).

[Accurate mass, m/z]: $\{\text{FeL}_3\text{T}\}^{2+}$ = 545.2005, $\{\text{FeL}_3\text{T}\}(\text{BF}_4)^+$ = 1177.4044. Elemental analysis (%) calculated for $\text{C}_{63}\text{H}_{54}\text{B}_2\text{F}_8\text{FeN}_{16} \cdot 1.15 \text{CHCl}_3 \cdot 1.8 \text{C}_2\text{H}_3\text{N}$: C 55.12, H 4.13, N 16.89; found: C 55.20, H 4.46, N 16.57.

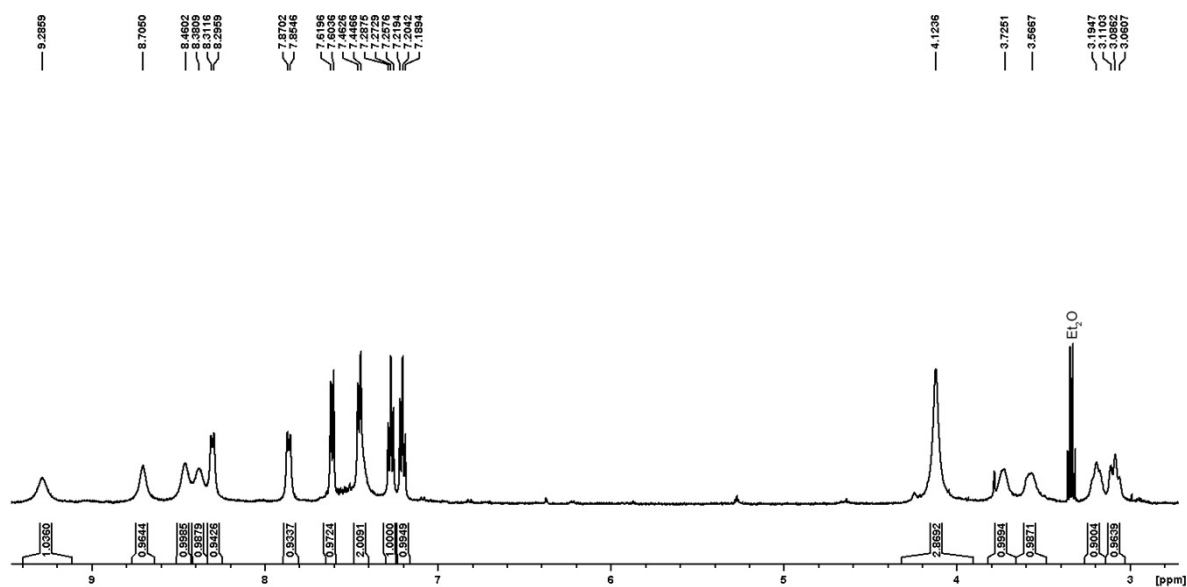


Figure S9: ^1H NMR (500 MHz, CD_3CN , 298 K) spectrum of diamagnetic complex **2**. Peak broadening is attributed to the chemical exchange of CH_2 protons of TREN as previously reported.⁴

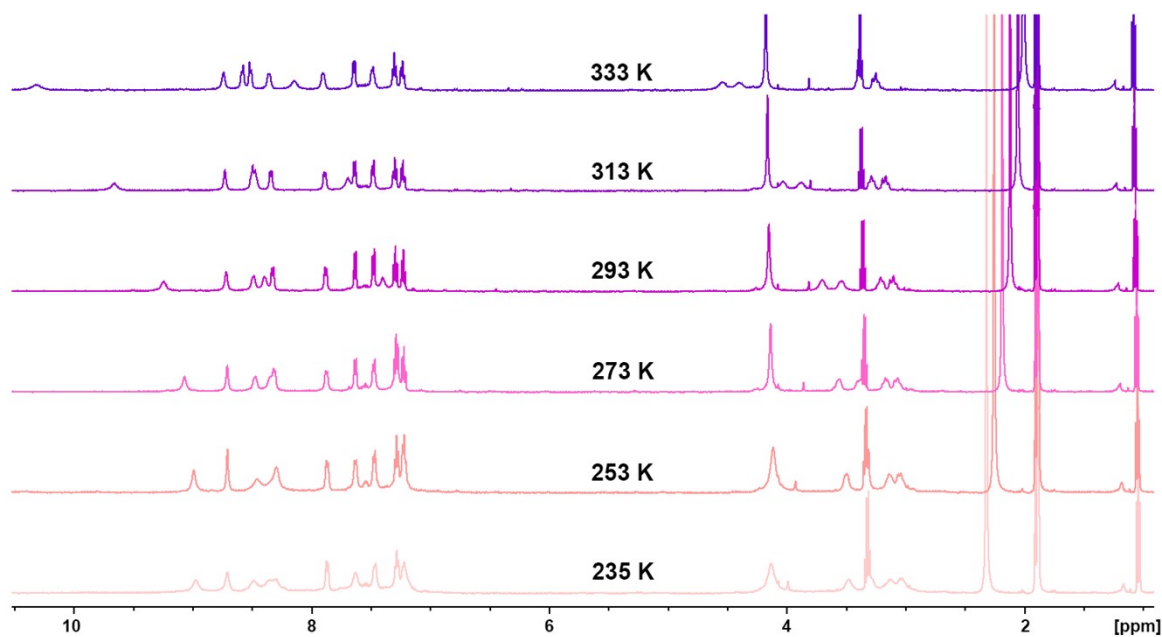


Figure S10: ^1H NMR (500 MHz, CD_3CN) spectra for complex **2** recorded at temperatures from 235 K (bottom) to 333 K (top) in five steps of 20 K.

S1.3.3 Complex 3: $[\text{Fe}_6\text{F}_6\text{L}_6\text{T}_2](\text{BF}_4)_7$

Ligand **L** (30.3 mg, 96.5 μmol , 6 equiv), $\text{Fe}(\text{BF}_4)_2 \cdot 6\text{H}_2\text{O}$ (32.6 mg, 96.5 μmol , 6 equiv) and tris-2(aminoethyl)amine (4.8 μL , 32.16 μmol , 2 equiv) were dissolved in acetonitrile (3 mL) giving a bright blue solution. This was heated (50°C, 24 hr) and the purple solution was layered with diethyl ether. The resulting purple solid was filtered and washed with chloroform to give a purple crystalline solid (38.2 mg, 12.2 μmol , 38%). DOSY diffusion coefficient: $6.32 \times 10^{-10} \text{ m}^2 \text{ s}^{-1}$. [Accurate mass, m/z]: $\{\text{Fe}_6\text{L}_6\text{F}_6\text{T}_2\}^{7+} = 359.93$ $\{\text{Fe}_6\text{L}_6\text{F}_6\text{T}_2(\text{BF}_4)\}^{6+} = 434.42$, $\{\text{Fe}_6\text{L}_6\text{F}_6\text{T}_2(\text{BF}_4)_2\}^{5+} = 538.71$, $\{\text{Fe}_6\text{L}_6\text{F}_6\text{T}_2(\text{BF}_4)_3\}^{4+} = 694.89$, $\{\text{Fe}_6\text{L}_6\text{F}_6\text{T}_2(\text{BF}_4)_4\}^{3+} = 955.52$, $\{\text{Fe}_6\text{L}_6\text{F}_6\text{T}_2(\text{BF}_4)_5\}^{2+} = 1476.78$. Elemental analysis (%) calculated for $\text{C}_{126}\text{H}_{108}\text{B}_7\text{F}_{34}\text{Fe}_6\text{N}_{32} \cdot 1.75 \text{CHCl}_3$: C 47.71, H 3.55, N 13.94; found: C 47.20, H 3.73, N 14.45.

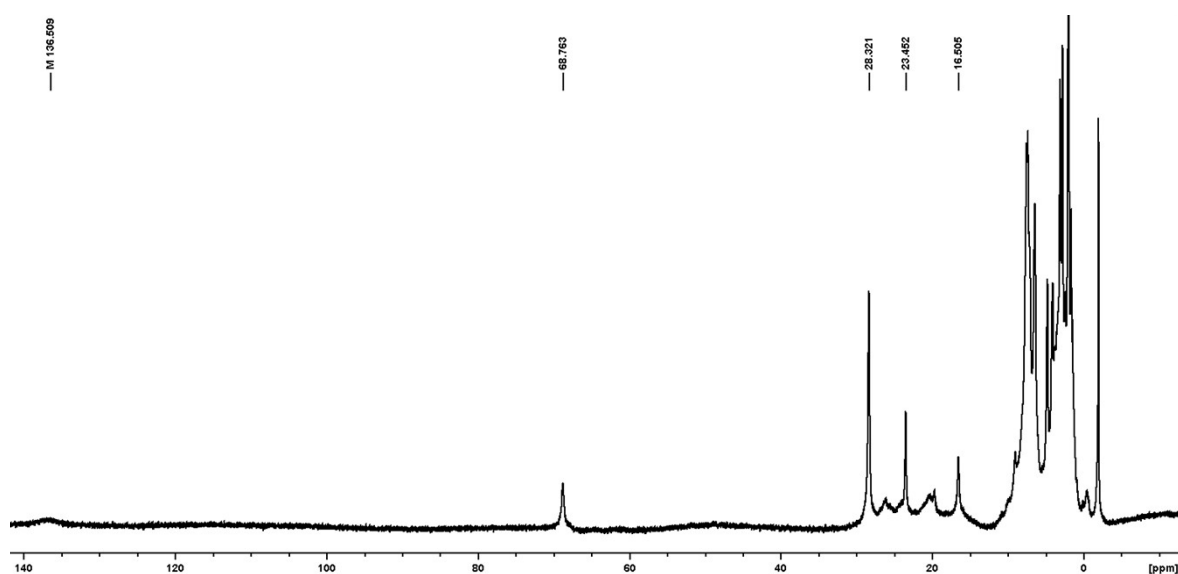


Figure S11: ^1H NMR (500 MHz, CD_3CN , 298 K) spectrum of complex **3**.

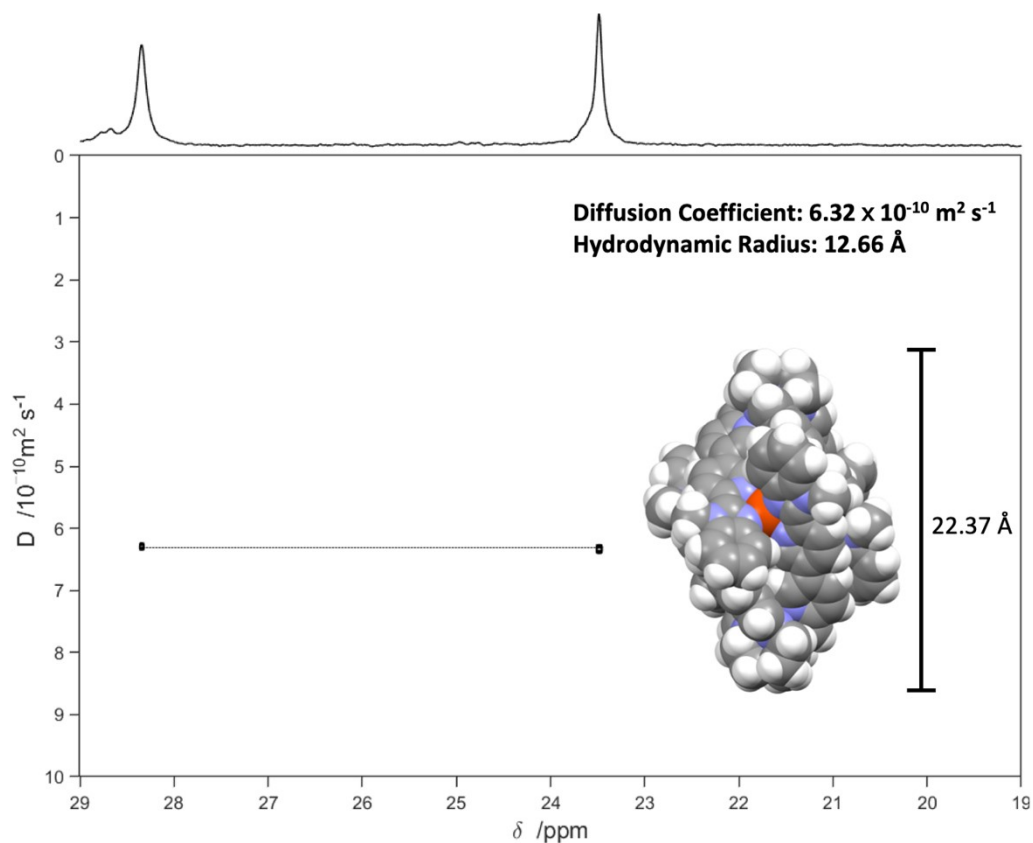


Figure S12: ^1H DOSY NMR (500 MHz, CD_3CN , 298 K) spectrum of complex **3**, highlighting two distinct peaks between 19 and 29 ppm.

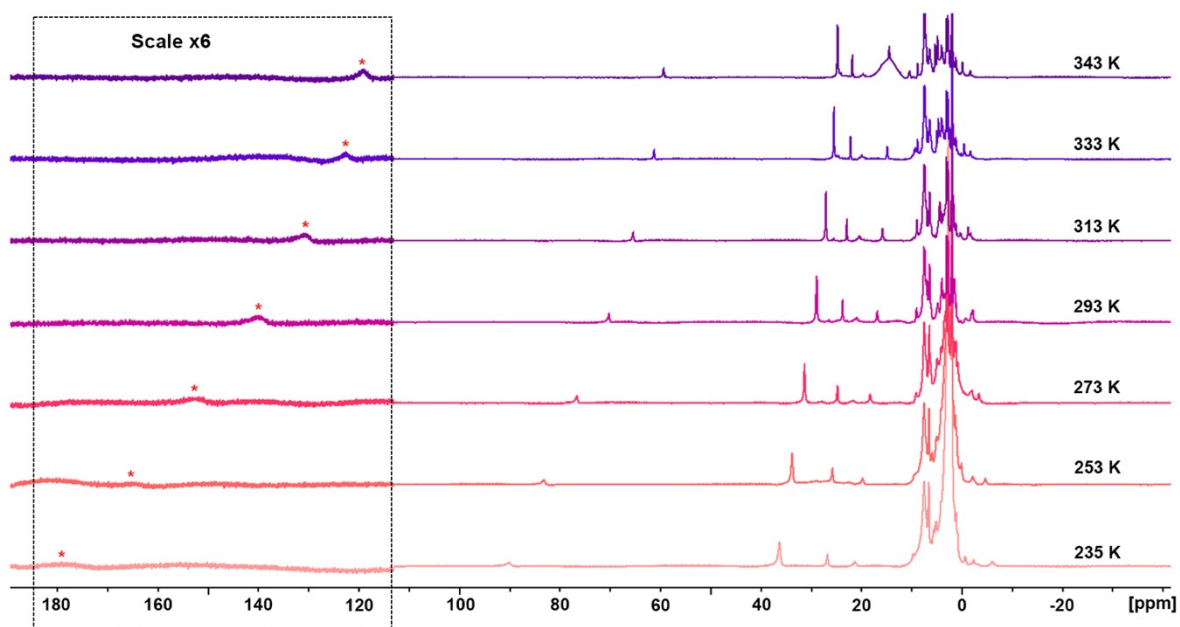


Figure S13: ^1H NMR (500 MHz, CD_3CN) spectra for complex **3** recorded at temperatures from 235 K (bottom) to 343 K (top) in five steps of 20 K and one of 10 K.

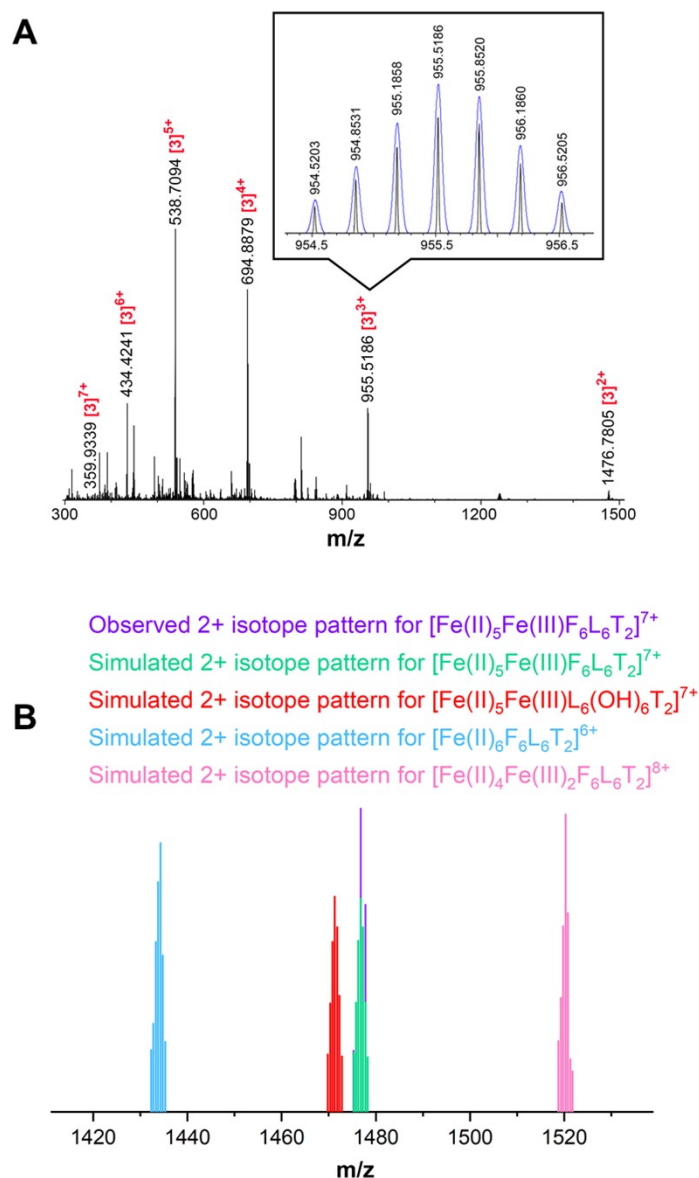


Figure S14: **A:** High-resolution mass spectrum for an acetonitrile solution of **3**. Inset the isotopic pattern for the $[\mathbf{3}]^{3+}$ peak, with the simulated isotopic pattern overlaid in blue. **B:** Isotopic distribution pattern for $[\mathbf{3}]^{2+}$; experimentally observed values are shown in purple alongside simulated values for complex **3** (green). Simulated values are also given for a complex in which all six fluoride ions are replaced with bridging hydroxides (red), where all six iron centres are found in the Fe(II) oxidation state (blue), and where the complex contains four irons as Fe(II) and two irons as Fe(III) (pink). The simulated isotope patterns in red, blue and pink all deviate significantly from the experimentally observed value. Variable numbers of tetrafluoroborate counterions balance the charge with the metal centres, sequential loss of these counterions gives rise to the series of peaks observed in Figure S14A. For all patterns observed in the mass spectrum of complex **3**, model values were calculated with enviPat Web 2.4.⁵

S1.3.4 Fe₄L₆ Tetrahedron with *p*-Toluidine

Ligand **L** (2.8 mg, 8.9 μmol, 6 equiv), *p*-toluidine (0.96 mg, 8.9 μmol, 6 equiv) and Fe(OTf)₂·6H₂O (2.2 mg, 5.9 μmol, 4 equiv) were dissolved in acetonitrile (0.5 mL) and the resulting purple solution was added to a J-Young NMR tube. The tube was sealed, and the solution was degassed by three vacuum/N₂ fill cycles before being heated (50°C, 24 hr). [Accurate mass, *m/z*]: {Fe₄L₆(*p*-Tol)₆(BF₄)₃}⁷⁺ = 398.89, {Fe₄L₆(*p*-Tol)₆(BF₄)₂}⁶⁺ = 490.45, {Fe₄L₆(*p*-Tol)₆(BF₄)₃}⁵⁺ = 618.13, {Fe₄L₆(*p*-Tol)₆(BF₄)₄}⁴⁺ = 819.15, {Fe₄L₆(*p*-Tol)₆(BF₄)₅}³⁺ = 1129.86, {Fe₄L₆(*p*-Tol)₆(BF₄)₆}²⁺ = 1769.26.

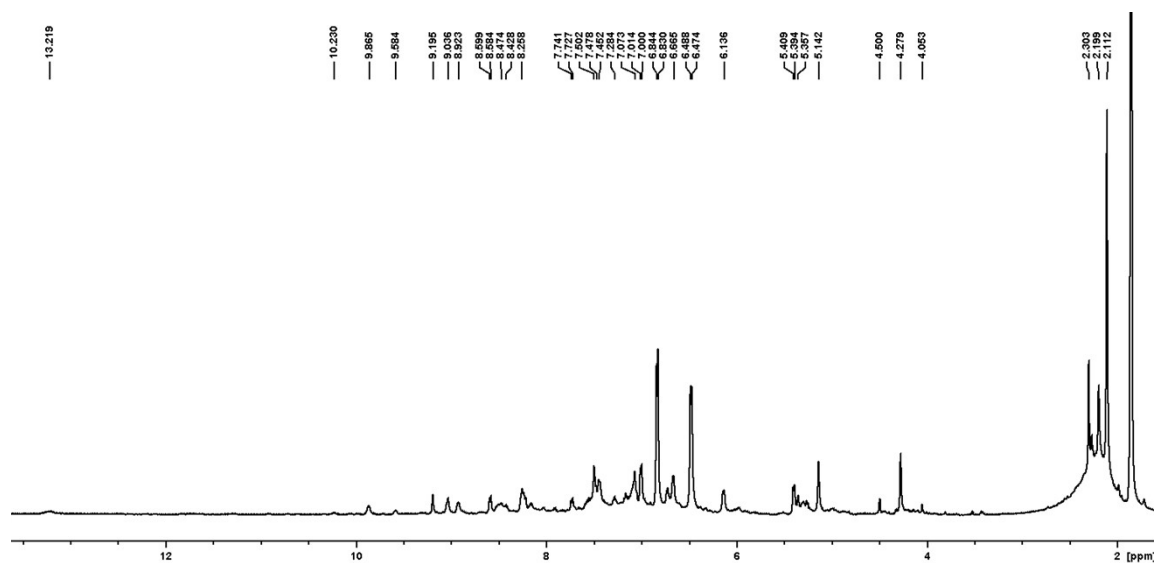


Figure S15: ¹H NMR (500 MHz, CD₃CN, 298 K) spectrum of the Fe₄L₆ tetrahedron formed with ligand **L**, *p*-toluidine and Fe(OTf)₂. The complicated ¹H NMR spectrum is attributed to the asymmetric ligand, which generates three isomers when arranged in a tetrahedral structure (Figure S15) giving rise to seven distinct imine environments before consideration of diastereoisomers.

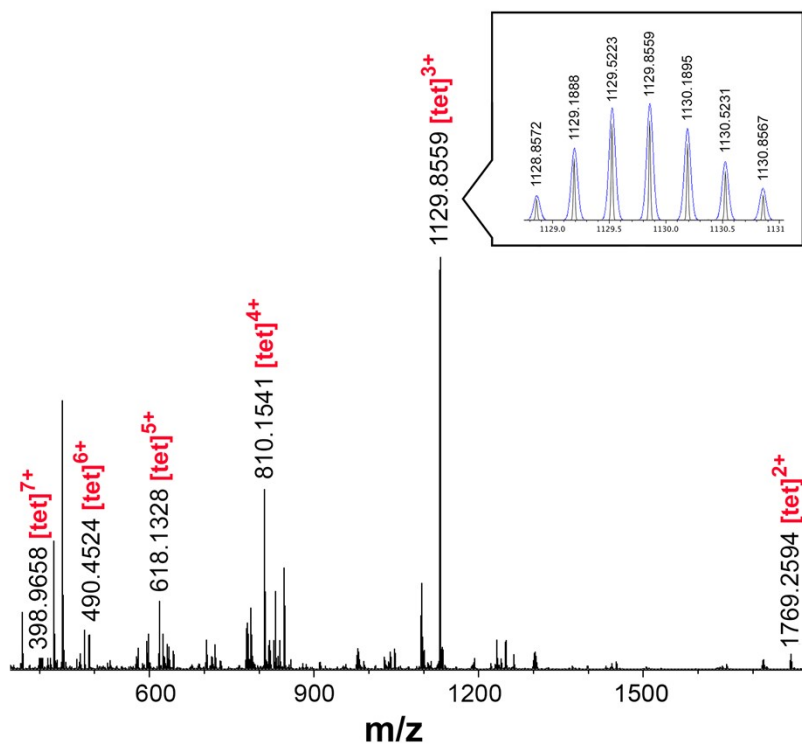


Figure S16: High-resolution mass spectrum for an acetonitrile solution of the Fe_4L_6 tetrahedron [tet]. Insert shows a zoom of the $[\text{tet}]^{3+}$ isotopic pattern, with the simulated isotopic pattern overlaid in blue.

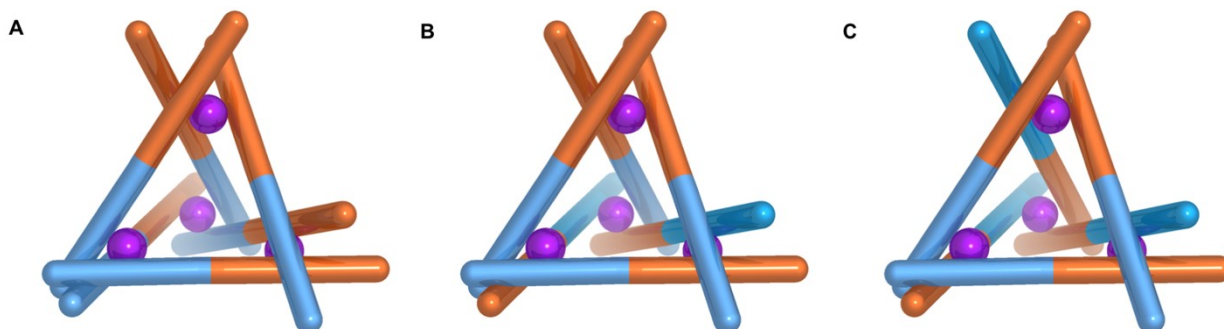


Figure S17: Models of the three possible isomeric structures formed with ligand **L**, *p*-toluidine and $\text{Fe}(\text{OTf})_2$. Orange and blue represent the different bidentate binding sites on the asymmetric ligand.

S2 X-Ray Crystallography

Data Collection. Single crystals of 2-(5-bromopyridin-2-yl)-1-methyl-1*H*-benzo[*d*]imidazole and protected ligand **L'** were obtained through the slow evaporation of chloroform to yield colourless crystals. X-ray data for 2-(5-bromopyridin-2-yl)-1-methyl-1*H*-benzo[*d*]imidazole were collected at 150(2) K using an Oxford Diffraction XCalibur II four circle diffractometer with an Atlas CCD detector and an enhance graphite-monochromated Mo K α radiation source ($\lambda = 0.71073$ Å). X-ray data for **L'** was collected at 150(2) K using an Agilent SuperNova four circle diffractometer with an Eos CCD detector and SuperNova microfocussed Mo K α radiation source ($\lambda = 0.71073$ Å). X-ray data for complex **1** was collected at 150(2) K using a Rigaku FR-X four circle diffractometer with a Hypix-6000HE HPC detector and FR-X microfocussed rotating anode Cu K α radiation source ($\lambda = 1.54146$). X-ray data for ligand **L** and compounds **2** and **3** were collected at a temperature of 100 K using a synchrotron radiation at the single crystal X-ray diffraction beamline I19 in Diamond Light Source,⁶ equipped with a Pilatus 2M detector and an Oxford Cryosystems nitrogen flow gas system. Data were measured using GDA suite of programs.

Crystal Structure Determinations and Refinements. X-ray data were processed and reduced using CrysAlisPro.⁷ Absorption correction was performed using empirical methods (SCALE3 ABSPACK) based upon symmetry-equivalent reflections combined with measurements at different azimuthal angles. The crystal structure was solved and refined against all F^2 values using the SHELX and Olex2 suite of programmes.^{8,9,10} All atoms were refined anisotropically. Hydrogen atoms were placed in calculated positions and refined using idealised geometries and assigned fixed isotropic displacement parameters.

Protected ligand **L'** co-crystallised with 5% starting material 2-(5-bromopyridin-2-yl)-1-methyl-1*H*-benzo[*d*]imidazole. Atomic displacement parameters of the molecule were restrained using SIMU SHELX commands. For complex **1**, atomic displacement parameters were restrained using a rigid body approach by applying SHELX RIGU commands and to be similar using SHELX SIMU commands. For complex **2**, the BF $_4^-$ anions were modelled to have ideal geometry, and the occupancy of the BF $_4^-$ anions were refined and constrained to be 2. The B-F distances were restrained to be similar using SHELX SADI commands. Atomic displacement parameters were restrained using a rigid body approach by applying SHELX RIGU commands and to be similar using SHELX SIMU commands.

For complex **3**, BF₄ anions were constrained to have idealized BF₄ structure and were placed on tetrahedral electron density regions as shown in Figure S22. One BF₄ anion was found to be disordered over two positions with a 50/50 occupancy. The overall occupancies of the BF₄ anions were refined, obtaining three fully occupied BF₄ positions and one BF₄ with a 50% occupancy in the asymmetric unit. Then, the occupancies were set to be 100 and 50%, respectively. Atomic displacement parameters were restrained using a rigid body approach by applying SHELX RIGU commands and to be similar using SHELX SIMU commands.

Packing of large molecules as proteins,¹¹ molecular knots,¹² cages,¹³ rotaxanes¹⁴ and metal-organic frameworks¹⁵ present large voids filled with ill-shaped electron density, corresponding to highly disordered solvent molecules. The Solvent Mask protocol implemented in OLEX 2 was applied to account for the poorly defined electron density remaining in the voids of crystal structures of **2** and **3** (figure S22). 220.2 electrons were found in two different voids in compound **2**, which could correspond to three diethyl ether molecules and two acetonitrile molecules in void 1, and two acetonitrile molecules in void 2. 902 electrons were found in one void for compound **3**, which could correspond to either 42 acetonitrile, 21 diethyl ether or 8 chloroform molecules. Mercury, Discovery Studio and PovRay were used for molecular graphics.^{16, 17, 18}

Crystallographic data have been deposited with the CCDC (CCDC 1952397 – 1952402, 2101118).

Table S1: Crystallographic data for molecules 2-(5-bromopyridin-2-yl)-1-methyl-1*H*-benzo[*d*]imidazole, L' and L.

	2-(5-bromopyridin-2-yl)-1-methyl-1<i>H</i>-benzo[<i>d</i>]imidazole	L'	L
Formula	C ₁₃ H ₁₀ BrN ₃	C _{20.62} H _{19.53} Br _{0.05} N _{3.96} O _{1.90}	C ₁₉ H ₁₄ N ₄ O
Fw	288.15	356.88	314.34
Cryst size, mm	0.2 x 0.2 x 0.08	0.2 x 0.2 x 0.2	0.2 x 0.2 x 0.1
Cryst syst	monoclinic	triclinic	triclinic
Space group	<i>P</i> 12 ₁ / <i>n</i> 1	<i>P</i> -1	<i>P</i> -1
a, Å	11.4679 (11)	8.3959(14)	7.2185(6)
b, Å	3.8858 (4)	10.4913(17)	8.4349(7)
c, Å	24.8130 (3)	10.5635(18)	13.3131(7)
α, °	90	75	73
β, °	96	86	88
γ, °	90	80	68
V, Å ³	1099.8(2)	886.0(3)	718.6(11)
Z	4	2	2
ρ _{calcd} , g cm ⁻³	1.740	1.338	1.453
μ, mm ⁻¹	3.715	0.201	0.089
No. of reflections made	7336	4679	15467
No. of unique reflns, R _{int}	2657, 0.0768	3224, 0.0449	6580, 0.0649
No. of reflns with F ² >2σ(F ²)	1786	2028	4030
Transmn coeff range	0.860-1.000	0.730-1.000	0.367-1.000
R, R _w ^a (F ² > 2σ(F ²))	0.0696, 0.1151	0.0797, 0.1992	0.0735, 0.1884
R, R _w ^a (all data)	0.1171, 0.1324	0.1154, 0.2417	0.1111, 0.2089
S ^a	1.063	1.070	0.976
Parameters	155, 0	245, 6	218, 0
Max, min, diff map, e Å ⁻³	1.148, -0.564	0.600, -0.751	0.669, -0.462

^a Conventional R = $\Sigma||F_o| - |F_c||/\Sigma|F_o|$; R_w = $[\Sigma w(F_o^2 - F_c^2)^2/\Sigma w(F_o^2)^2]^{1/2}$; Σ = $[\Sigma w(F_o^2 - F_c^2)^2/\text{no. data} - \text{no. params}]^{1/2}$ for all data.

Table S2: Crystallographic data for complexes **1**, **2** and **3**.

	1	2	3
Formula	C _{61.62} H _{49.07} B ₂ F _{7.84} FeN _{14.07} O ₃	C ₆₃ H ₅₄ B ₂ F ₈ FeN ₁₆	C ₁₂₆ H ₁₀₈ B ₇ F ₃₄ Fe ₆ N ₃₂
Fw	1261.14	1264.69	3127.21
Cryst size, mm	0.1 x 0.1 x 0.1	0.03 x 0.02 x 0.01	0.26 × 0.17 × 0.15
Cryst syst	triclinic	triclinic	trigonal
Space group	<i>P</i> -1	<i>P</i> -1	<i>P</i> 3 ₁ 21
a, Å	10.5589(7)	15.105(3)	26.679(3)
b, Å	14.5471(9)	15.136(2)	26.679(3)
c, Å	21.5140(12)	19.131(3)	21.8284(11)
α, °	72	74	90
β, °	82	70	90
γ, °	70	61	120
V, Å ³	2953.7(4)	3562.6(12)	13455(3)
Z	2	2	3
ρ _{calcd} , g cm ⁻³	1.418	1.179	1.158
μ, mm ⁻¹	0.340	2.276	0.506
No. of reflections made	24792	40026	84019
No. of unique reflns, R _{int}	13157, 0.0426	14501, 0.1226	16361, 0.1039
No. of reflns with F ² >2σ(F ²)	8895	6112	7658
Transmn coeff range	0.922-1.000	0.897-1.000	0.691-1.000
R, R _w ^a (F ² > 2σ(F ²))	0.0896, 0.2300	0.0955, 0.2538	0.0789, 0.2135
R, R _w ^a (all data)	0.1325, 0.2558	0.1780, 0.3085	0.1572, 0.2678
S ^a	1.052	0.952	0.969
Parameters	877, 448	766, 152	1155, 960
Max, min, diff map, e Å ⁻³	1.262, -0.599	1.166, -0.532	0.63, -0.38

^a Conventional R = $\sum||F_o| - |F_c||/\sum|F_o|$; R_w = $[\sum w(F_o^2 - F_c^2)^2 / \sum w(F_o^2)^2]^{1/2}$; S = $[\sum w(F_o^2 - F_c^2)^2 / \text{no. data} - \text{no. params}]^{1/2}$ for all data.

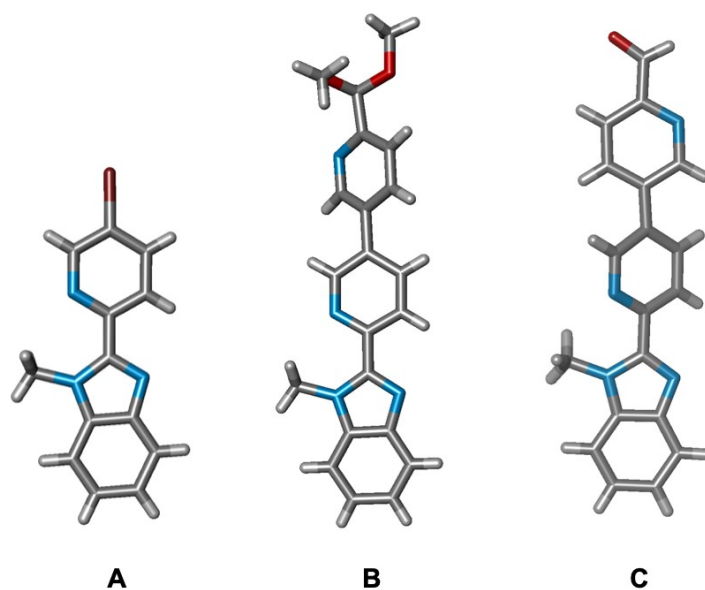


Figure S18: Single-crystal X-ray structures of **A**: starting material 2-(5-bromopyridin-2-yl)-1-methyl-1*H*-benzo[*d*]imidazole; **B**: protected ligand **L'** and **C**: target ligand **L**.

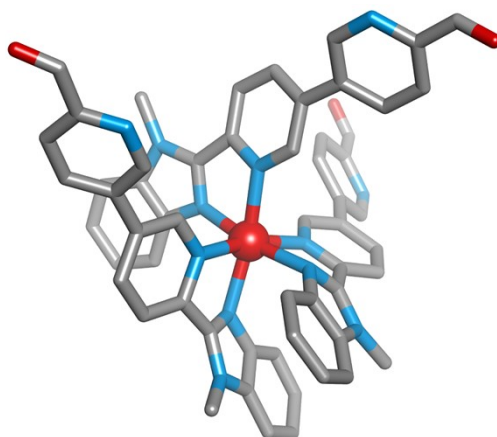


Figure S19: Single-crystal X-ray structure of structure of complex **1**. The counterions and hydrogen atoms are omitted for clarity.

The crystal structure obtained for complex **1** does not necessarily represent the major structure in solution. Although the *mer* isomer was characterised in figure S19, there is evidence in the ^1H NMR spectrum for the presence of both the *mer* and *fac* isomers in the solution state. In the mass spectrum there is evidence of substoichiometric complexes such as $[\text{FeL}_2]^{2+}$, which could also exist in solution alongside complex **1**.

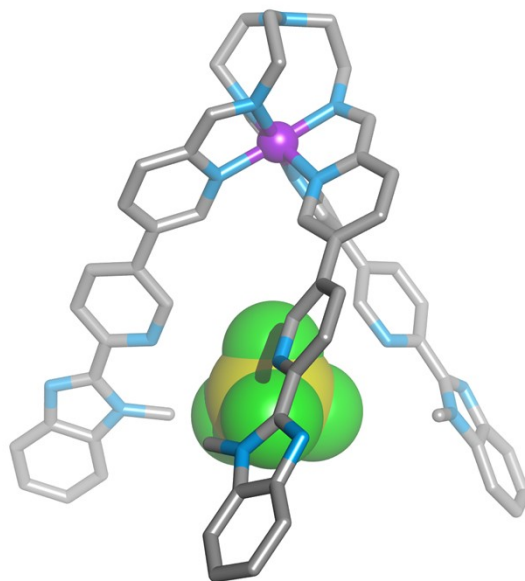


Figure S20: Single-crystal X-ray structure of complex **2**. BF_4^- counterions were distributed across three positions in the crystal lattice, one of which was on the three-fold rotation axis of the complex (occupancy $\sim 75\%$). The occupancy of the BF_4^- counterions were refined and constrained to be two. The additional counterion and hydrogen atoms are omitted for clarity.

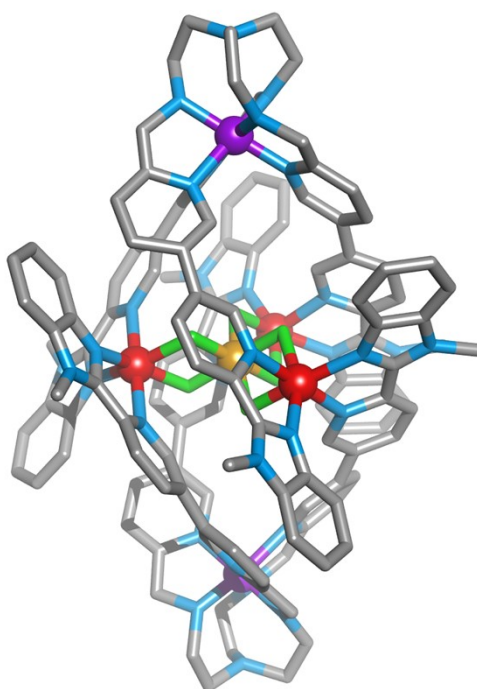


Figure S21: Single-crystal X-ray structure of complex **3**, where purple: low-spin iron(II); red: high-spin iron(II), yellow: iron(III), green: fluoride ions; blue: nitrogen; grey: carbon. The counterions and hydrogen atoms are omitted for clarity.

Table S3: Crystallographically characterised bond angles between the central Fe⁵ ion and the connected Fe³ and Fe⁴ ions through the bridging fluoride atoms in complex **3**.

Atoms	Bond Angle (°)
Fe ³ – F ¹ – Fe ⁵	103.5(3)
Fe ⁴ – F ² – Fe ⁵	101.9(3)
Fe ⁴ – F ³ – Fe ⁵	102.2(3)

Table S4: Crystallographically characterised bond lengths between the central Fe⁵ ion and the six bonded fluoride atoms in complex **3**.

Atoms	Bond Length (Å)
Fe ⁵ – F ¹	1.922(8)
Fe ⁵ – F ¹	1.922(8)
Fe ⁵ – F ²	1.932(5)
Fe ⁵ – F ²	1.932(5)
Fe ⁵ – F ³	1.898(8)
Fe ⁵ – F ³	1.898(8)

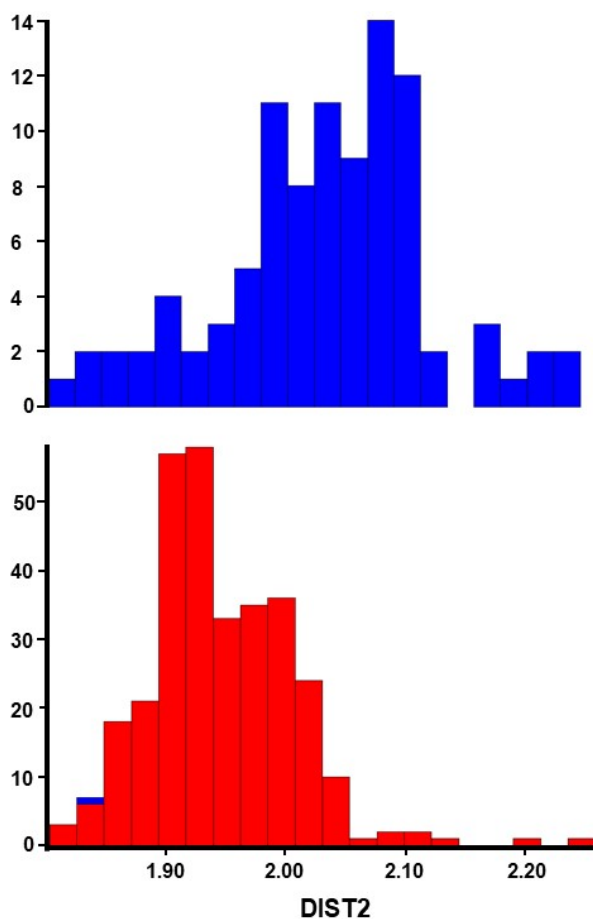


Figure S22: Top (blue): Histogram for Fe(II)-F bond distances excluding μ_3 -F-Fe structures. Bottom (red): Histogram for Fe(III)-F bond distances excluding μ_3 -F-Fe structures. Based on the CCDC data on crystal structures containing Fe(II)-F and Fe(III)-F bonds (excluding μ_3 -F-Fe), data for complex **3** is entirely consistent with our assignment of the Fe⁵ atom as an Fe(III) ion.

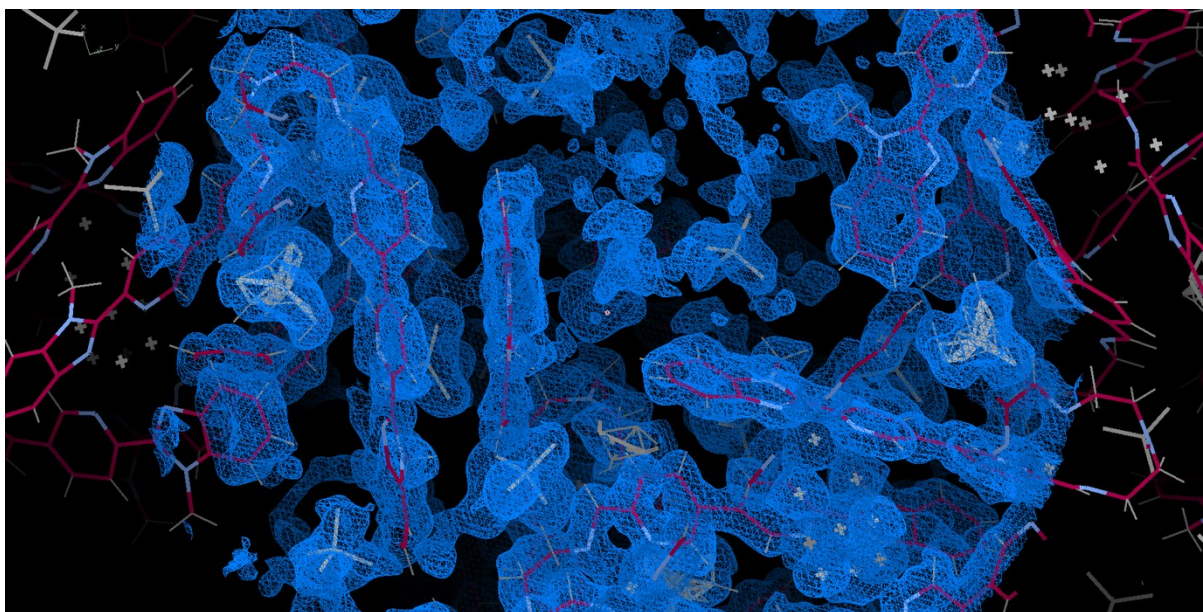


Figure S23: 2Fo-Fc electron density map representation of compound **3**. Electron density map pictures (4 msd) is represented in blue, carbon atoms are represented in red, nitrogen in light blue, BF₄ in grey and iron in white crosses. 2Fo-Fc electron density maps were obtained using Phenix software. Initially, the reflections file (.mtz) obtained from CrysAlisPro were edited to include the map coefficients. Then, the maps were calculated from the edited reflections file and the model (pdb file) obtained from structure solution software (OLEX 2) using phenix.maps software.

S3 Bond Valence Sum (BVS) Analysis

Bond valence sum analysis is a method widely used throughout coordination chemistry to support assignment of oxidation states at metal centres. Bond valence parameters are established from structural data, often obtained from the Cambridge Structural Database (CSD).¹⁹

Equation 1 describes the relationship between bond valence (S_{ij}) and bond length (r_{ij}) based on cation i and anion j .²⁰ Both r_0 and B are parameters of empirical origin, where r_0 is specific to a particular ionic pair, and B is a constant assigned the value 0.37 \AA .¹⁹

$$S_{ij} = \exp\left(\frac{r_0 - r_{ij}}{B}\right) \quad (1)$$

The Fe^{II} -N bond distances are indicative of the spin-state of iron(II) metal centres. In 2017, Zheng and co-workers examined the literature and refined r_0 values for Fe^{II} -N bonds, enabling distinct values for both low-spin (LS) and high-spin (HS) centres to be tabulated. The appropriate r_0 values are reported in table S5.

Table S5: Calculated r_0 values for both low-spin and high-spin iron(II) centres.¹⁹

Fe^{II} Spin State	r_0 (Å)
Low spin	1.57
High spin	1.76

S3.1 Complex 1

For complex **1**, the spin state of the iron(II) centre bound at the benzimidazole binding site was investigated using the BVS analysis method.

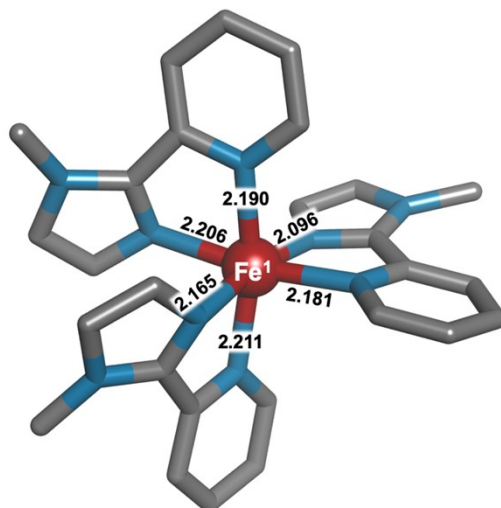


Figure S24: Image of the Fe¹ centre in **1** obtained from the single-crystal X-ray structure where red: high-spin iron(II); blue: nitrogen; grey: carbon. Atoms above the pyridyl-imine ring were omitted for clarity. All Fe-N bond lengths are reported in Å.

As seen in figure S19, the iron(II) centre is bound octahedrally to six nitrogen atoms. Using the crystallographically obtained bond lengths for **1**, S_{ij} values were calculated for the iron(II) centre in both the HS and LS state (Table S6).

S_{ij} values were calculated using equation 1, and the valence (V_i), which corresponds to the oxidation state of the metal centre, was calculated using equation 2.

$$V_i = \sum_j S_{ij} \quad (2)$$

Table S6: Crystallographically characterised bond lengths between the Fe^I ion and nitrogen donors in complex **1**.

Fe ^I -N (Å)	S _{ij} Fe ^{II} -N (LS)	S _{ij} Fe ^{II} -N (HS)
2.190(17)	0.187	0.313
2.096(4)	0.241	0.403
2.181(4)	0.192	0.321
2.211(3)	0.177	0.296
2.165(4)	0.200	0.335
2.206(4)	0.179	0.300
Average = 2.17	V_i = 1.18	V_i = 1.97

Based on the crystallographically characterised bond lengths listed in table S6, the BVS analysis data supports that the iron(II) centre in complex **1** is high-spin.

S3.2 Complex 2

The spin state of the iron(II) centre bound in the pyridyl-imine binding site of complex **2** was also investigated using the BVS analysis method.

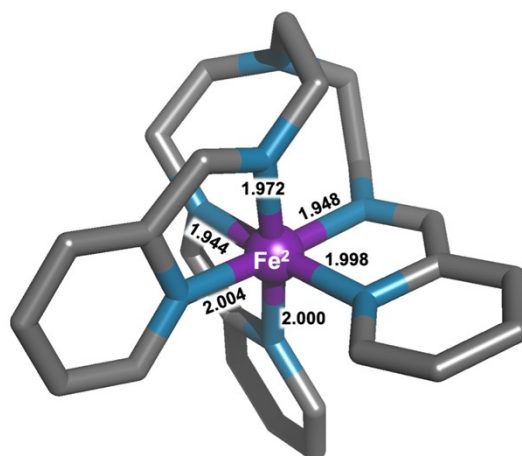


Figure S25: Image of the Fe²⁺ centre in **2** obtained from the single-crystal X-ray structure where purple: low-spin iron(II); blue: nitrogen; grey: carbon. Atoms below the pyridyl-imine ring were omitted for clarity. All Fe-N bond lengths are reported in Å.

Table S7: Crystallographically characterised bond lengths between the Fe² ion and nitrogen donors in complex **2**.

Fe ² -N (Å)	S _{ij} Fe ^{II} -N (LS)	S _{ij} Fe ^{II} -N (HS)
1.972(5)	0.337	0.564
1.948(5)	0.360	0.602
1.998(2)	0.315	0.526
2.000(3)	0.313	0.523
2.004(3)	0.309	0.517
1.944(5)	0.364	0.608
Average = 1.98	V_i = 2.00	V_i = 3.34

Based on the crystallographically characterised bond lengths listed in table S7, the BVS analysis data supports that the iron(II) centre in complex **2** is low-spin.

S3.3 Complex 3

For complex **3** four separate iron environments were observed crystallographically, we have assigned them Fe², Fe³, Fe⁴, and Fe⁵.

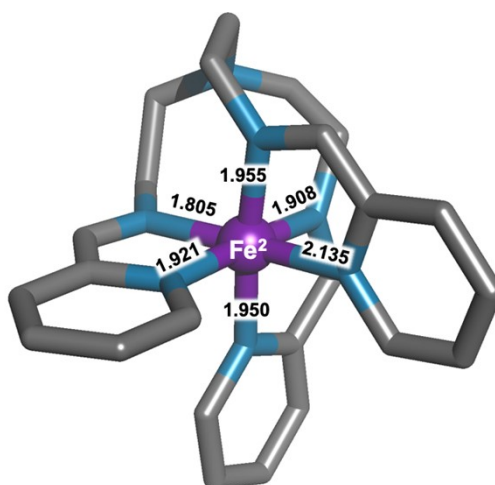


Figure S26: Image of the Fe² centre in **3** obtained from the single-crystal X-ray structure purple: low-spin iron(II); blue: nitrogen; grey: carbon. Atoms below the pyridyl-imine ring were omitted for clarity. All Fe-N bond lengths are reported in Å.

Table S8: Crystallographically characterised bond lengths between the Fe² ion and nitrogen donors in the pyridyl-imine binding sites in complex **3**.

Fe ² -N (Å)	S _{ij} Fe ^{II} -N (LS)	S _{ij} Fe ^{II} -N (HS)
1.963(13)	0.347	0.579
1.960(12)	0.349	0.582
1.981(11)	0.329	0.550
1.932(14)	0.376	0.628
1.951(13)	0.357	0.597
1.935(10)	0.373	0.623
Average = 1.95 Å	V_i = 2.13	V_i = 3.56

Based on the crystallographically characterised bond lengths listed in table S8, the BVS analysis data supports that the iron(II) centres bound in the pyridyl-imine binding sites in complex **3** are low-spin.

S3.3.1 High-Spin Fe(II)/Fe(III) Core

Since the electronic configuration of the iron ions is linked with the length of the Fe-N bonds (Table S5), the Fe-F bond lengths are similarly expected to vary based on their oxidation and spin-states. However, due to the limited number of reported Fe-F bonded structures the CSD contains insufficient data to generate reliable r_0 estimations for Fe-F bonds.¹⁹ The r_0 values for Fe^{II}-F bonds that are available are therefore undifferentiated in terms of spin-state and are assigned as $r_0 = 1.67 \text{ \AA}$, a value calculated by Zheng and co-workers based on all homo- and heteroleptic iron(II) sites found on the CSD.¹⁹

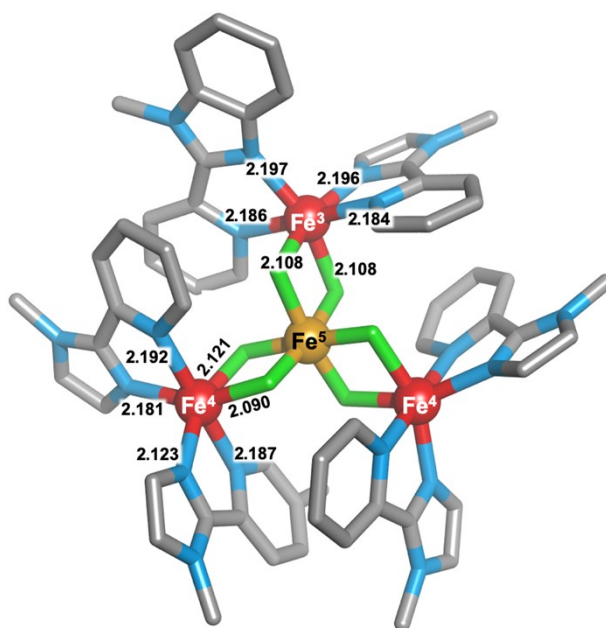


Figure S27: Image of the $[\text{Fe}^{\text{III}}(\mu\text{-F})_6(\text{Fe}^{\text{II}})_3]^{3+}$ core obtained from the single-crystal X-ray structure where red: high-spin iron(II), yellow: iron(III), green: fluoride ions; blue: nitrogen. All Fe-N/F bond lengths are reported in \AA .

Table S9: Crystallographically characterised bond lengths between Fe^3 and Fe^4 ions and nitrogen donors/fluoride ions in the $[\text{Fe}^{\text{III}}(\mu\text{-F})_6(\text{Fe}^{\text{II}})_3]^{3+}$ core.

Fe ³ bond lengths (\AA)		S _{ij} Fe ³ (LS)		S _{ij} Fe ³ (HS)		Fe ⁴ bond lengths (\AA)		S _{ij} Fe ⁴ (LS)		S _{ij} Fe ⁴ (HS)	
N	F	N	F	N	F	N	F	N	F	N	F
2.202(11)	2.048(7)	0.181	0.360	0.303	0.306	2.123(12)	2.089(8)	0.224	0.322	0.375	0.322
2.202(11)	2.048(7)	0.181	0.360	0.303	0.306	2.136(9)	2.112(6)	0.217	0.360	0.362	0.360
2.104(12)		0.236		0.395		2.189(15)		0.188		0.314	
2.104(12)		0.236		0.395		2.109(15)		0.233		0.389	
		V_i = 1.55		V_i = 2.11				V_i = 1.54		V_i = 2.12	

Based on the crystallographically characterised bond lengths listed in table S9, the BVS analysis data supports that the three iron(II) centres (Fe^{3+} , Fe^{4+}) in the core of complex **3** are high-spin.

S4 UV-Vis Spectroscopy

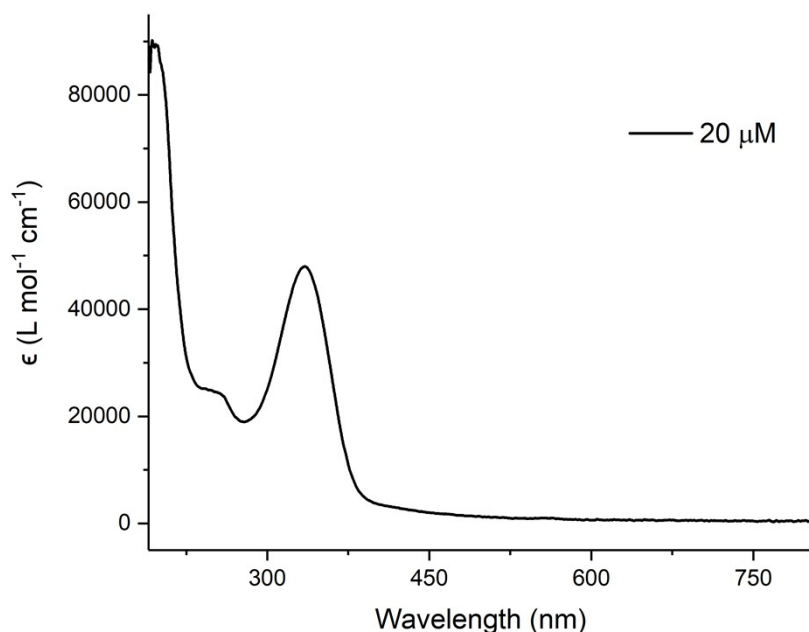


Figure S28: UV-Vis absorption spectrum of ligand **L** in acetonitrile (20 μM).

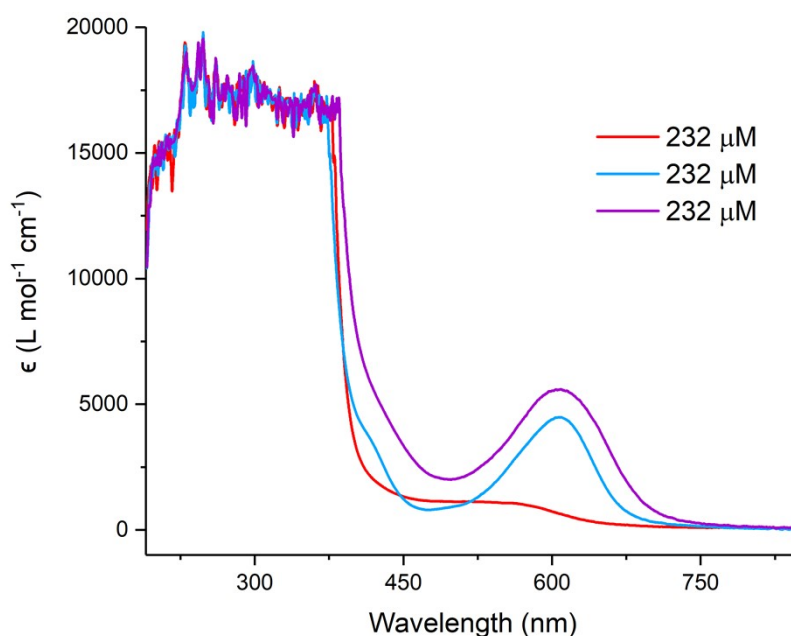


Figure S29: UV-Vis absorption spectrum of red: complex **1**, blue: complex **2** and purple: complex **3** in acetonitrile (232 μM). A characteristic MLCT transition for the $\text{Fe}(\text{II})$ trispyridylimine site can be seen at around 607 nm.^{21, 22}

S5 SQUID Magnetometry

Magnetic measurements were performed on powdered samples of **1** and **3** using a Quantum Design MPMS-XL7 SQUID magnetometer equipped with a 7 T magnet. Magnetic susceptibility data were recorded under applied fields of 1, 5 or 10 kG, over the temperature range 2-300 K. Prior to measurement, the finely ground crystalline samples were restrained in eicosane to avoid the reorientation of the sample in applied magnetic field. Experimental data were corrected for the diamagnetism of the compound by using tabulated Pascal constants and for the diamagnetism of the sample holder and eicosane by measurement.

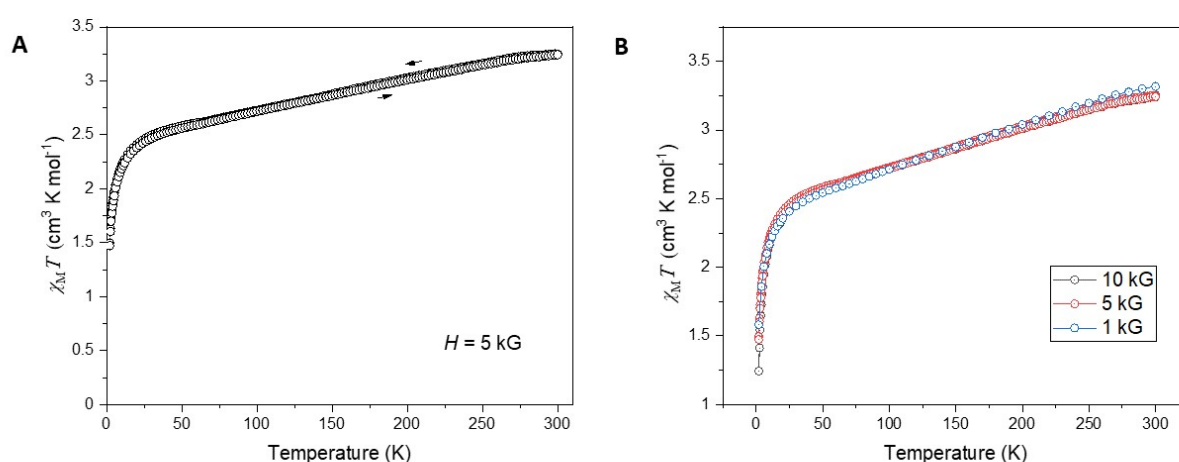


Figure S30: Plots of $\chi_M T$ vs T for **1** measured under cooling and warming regimes, at the temperature sweeping rate of 2 K/min and under applied fields of 1, 5 and 10 kG, and showing: A) the reversible nature of the spin-crossover (SCO) behavior, and B) the effect of field strength. Only a small fraction of the Fe(II) molecules (ca. 16%) undergo thermally induced spin crossover, while the large majority remains high-spin over the 2-300 K range.

Field dependent magnetization data for complex **3** were recorded at 2 and 4 K, by varying the magnetic field from 0 to 7 T. Possible slow relaxation of magnetization of **3** was investigated through measurements of the alternate-current (ac) magnetic susceptibility. Frequency dependence (1-1400 Hz) of the in-phase (χ_M') and out-of-phase (χ_M'') ac susceptibilities were recorded at fixed temperatures between 1.85 and 6.2 K, under applied dc fields of either 0 or 1000 Oe, and an ac field of 1.55 Oe varying at frequencies between 1 and 1400 Hz. The resulting $\chi_M T$ vs. T and M vs. H curves were fitted simultaneously using the program PHI²³

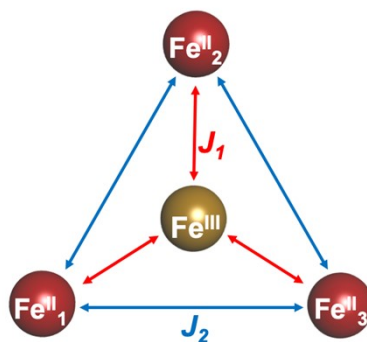
(version 3.1.1) by matrix diagonalisation of the (perturbative) anisotropic spin Hamiltonian defined in either equation (3) or (4):

$$\begin{aligned} \hat{H} = & \mu_B B \sum_i g_i \hat{S}_i - 2J_1 \left(\hat{S}_{Fe^{III}} \hat{S}_{Fe^{II}_1} + \hat{S}_{Fe^{III}} \hat{S}_{Fe^{II}_2} + \hat{S}_{Fe^{III}} \hat{S}_{Fe^{II}_3} \right) \\ & - 2J_2 \left(\hat{S}_{Fe^{II}_1} \hat{S}_{Fe^{II}_2} + \hat{S}_{Fe^{II}_2} \hat{S}_{Fe^{II}_3} + \hat{S}_{Fe^{II}_3} \hat{S}_{Fe^{II}_1} \right) + D_{Fe^{II}_i} \sum_i \left(\hat{S}_{z_{Fe^{II}_i}}^2 - \frac{\hat{S}_{Fe^{II}_i}^2}{3} \right) \end{aligned} \quad (3)$$

$$\hat{H} = \mu_B B \sum_i g_i \hat{S}_i - 2J_1 \left(\hat{S}_{Fe^{III}} \hat{S}_{Fe^{II}_1} + \hat{S}_{Fe^{III}} \hat{S}_{Fe^{II}_2} + \hat{S}_{Fe^{III}} \hat{S}_{Fe^{II}_3} \right) - 2zJ (\hat{S}_i \hat{S}_j) + D_{Fe^{II}_i} \sum_i \left(\hat{S}_{z_{Fe^{II}_i}}^2 - \frac{\hat{S}_{Fe^{II}_i}^2}{3} \right) \quad (4)$$

where \hat{S}_{Fe^N} ($S = 2$ for $N = II$ or $S = 5/2$ for $N = III$) represents the total spin operator of the individual iron ions within the cluster, B is the applied magnetic field, μ_B is the Bohr magneton, g is the isotropic g -factor of the compound, $D_{Fe^{II}_i}$ is the axial zero-field splitting term for high-spin iron(II) ions, while J_1 , J_2 and zJ are coupling constants measuring interactions between Fe(II) and Fe(III) ions (J_1), between neighbouring Fe(II) sites (J_2), and long-distance inter-cluster interactions (zJ), respectively. To avoid the overparameterization of the spin Hamiltonian, the anisotropy term of the Fe(III) site was assumed to be negligible, due to $3d^5$ (high-spin) configuration, and the g factor was fixed.

Scheme S3: Coupling scheme used for the modelling of magnetic data (Spin Hamiltonian eq. 3 and 4).



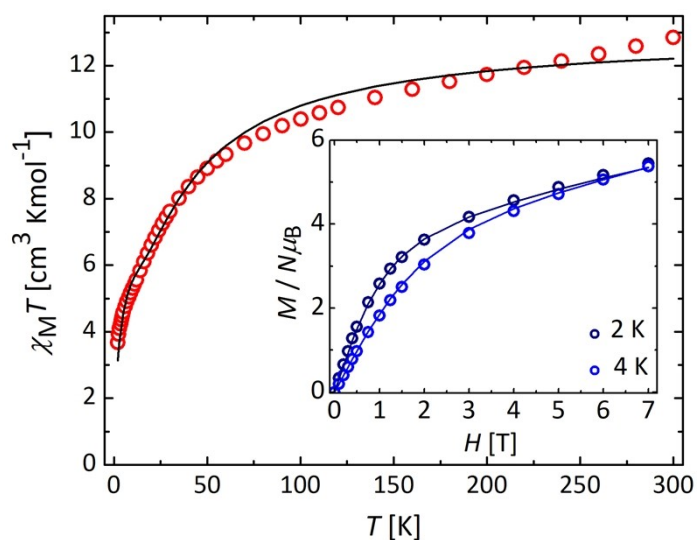


Figure S31: $\chi_M T$ vs T and M vs H (inset) curves of compound **3** with the best fit (solid line) employing the spin Hamiltonian defined in equation 4, and magnetic parameters listed in table S10 (Fit 2).

Table S10: Comparison of parameters and quality of four best fits ($\chi_M T$ vs T and $M/N_{\mu B}$ vs H) for the **3**.

Fit	Fitted parameters					Residual
	g	J_1 (cm ⁻¹)	J_2 (cm ⁻¹)	zJ (cm ⁻¹)	D (cm ⁻¹)	
1	1.97	-1.55	-0.17	-	8.93	0.101
2	1.97	-1.54	-	-0.011	9.94	0.157
3	1.99	-1.61	-0.21	-	9.19	0.123
4	1.99	-1.60	-	-0.014	10.46	0.200

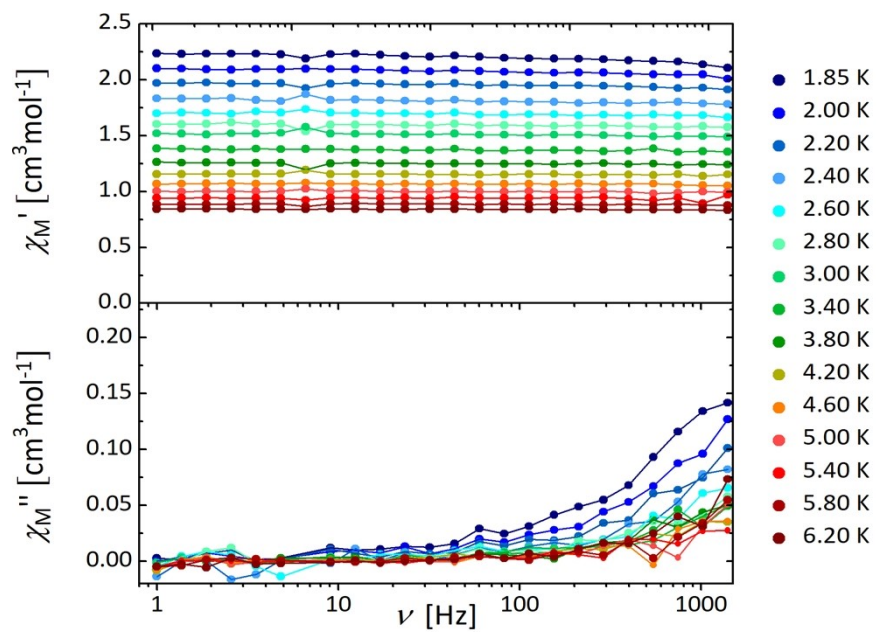


Figure S32: Frequency dependence of the in-phase (χ_M') and out-of-phase (χ_M'') ac susceptibility for **3** under an applied dc field of 1000 Oe. The solid lines are guides for the eye.

S6 EPR spectroscopy

EPR spectra were collected on a Bruker EMX 300 EPR spectrometer operated at 34 GHz (Q-band) microwave frequency and at variable temperatures.

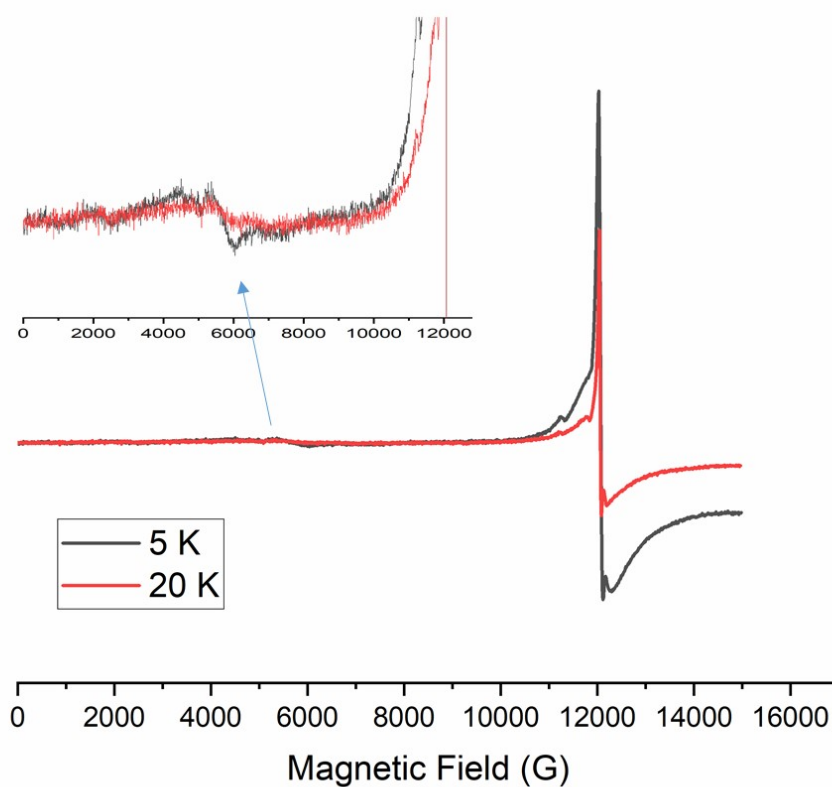


Figure S33: Q-band (34 GHz) EPR spectra at 5 and 20 K for a polycrystalline sample of **3**.

S7 References

1. L. Castañar, G. Dal Poggetto, A. A. Colbourne, G. A. Morris, M. Nilsson, *Magn. Reson. Chem.*, 2018, **56**(6), 546-558
2. R. Evans, Z. Deng, A. K. Rogerson, A. S. McLachlan, J. J. Richards, M. Nilsson, G. A. Morris, *Angew. Chem.*, 2013, **125**(11), 3199-3202
3. R. Evans, G. Dal Poggetto, M. Nilsson, G. A. Morris, *Anal. Chem.*, 2018, **90**(6), 3987-3994
4. H. He, K. R. Rodgers, A. M. Arif, *J. Inorg. Biochem.*, 2004, **98**, 667-676
5. M. Loos, C. Gerber, F. Corona, J. Hollender and H. Singer, *Anal. Chem.*, 2015, **87**(11), 5738-5744
6. H. Nowell, S. A. Barnett, K. E. Christensen, S. J. Teat and D. R. Allan, *J. Synchrotron Radiat.*, 2012, **19**, 435-441.
7. CrysAlisPRO, Oxford Diffractions /Agilent Technologies UK Ltd, Tarnton, England.
8. G. M. Sheldrick, *Acta. Cryst.*, 2015, **A71**, 3-8.
9. G. M. Sheldrick, *Acta. Cryst.*, 2015, **C71**, 3-8.
10. O. V. Dolomanov, L. J. Bourhis, R. J. Gildea, J. A. K. Howard and H. Puschmann, *J. Appl. Cryst.*, 2009, **42**, 339-341.
11. P. V. Afonine, R. W. Grosse-Kunstleve, P. D. Adams and A. Urzhumtsev, *Acta. Cryst.*, **D69**, 2013, 625-634
12. J. J. Danon, A. Krüger, D. A. Leigh, J-F. Lemonnier, A. J. Stephens, I. J. Vitorica-Yrezabal and S. L. Woltering, *Science*, 2017, **355**, 159-162.
13. I. A. Riddell, M. M. J. Smulders, J. K. Clegg, Y. R. Hristova, B. Breiner, J. D. Thoburn, Jonathan R. Nitschke, *Nat. Chem.*, **4**, 2012, 751–756.
14. J. Ferrando-Soria, E. Moreno Pineda, A Chiesa, A. Fernandez, S. A. Magee, S. Carretta, P. Santini, I. J. Vitorica-Yrezabal, F. Tuna, G. A Timco, E. J.L. McInnes, R. E. P. Winpenny, *Nat. Commun*, 2016, **7**, 11377.
15. M. Souto, J. Romero, J. Calbo, I. J. Vitórica-Yrezabal, J. L. Zafra, J. Casado, E. Ortí, A. Walsh, G. Mínguez Espallargas, *J. Am. Soc. Chem.*, **140**, 2018, 10562-10569
16. C. F. Macrae, I. J. Bruno, J. A. Chisholm, P. R. Edgington, P. McCabe, E. Pidcock, L. Rodriguez-Monge, R. Taylor, J. van de Streek and P. A. Wood, *J. Appl. Cryst.*, 2008, **41**, 466-470.
17. Dassault Systèmes BIOVIA, *Discovery Studio Visualizer*, [v17.2.0.16349], San Diego: Dassault Systèmes, [2016].

18. Persistence of Vision Pty. Ltd., 2004, Persistence of Vision Raytracer (Version 3.6), [Computer software]. Retrieved from <http://www.povray.org/download/>.
19. H. Zheng, K. M. Langner, G. P. Shields, J. Hou, M. Kowiel, F. H. Allen, G. Murshudov and W. Minor, *Acta. Cryst.*, 2017, **D73**, 316-325.
20. E. Pidcock, 1995, 'Structural Considerations of d-Transition Metal Compounds', PhD thesis, The University of Manchester, Manchester.
21. N. Huse, T. K. Kim, L. Jamula, J. K. McCusker, F. M. F. de Groot and R. W. Schoenlein, *J. Am. Chem. Soc.*, 2010, **132**, 6809-6816
22. M. Hardy, N. Struch, F. Topić, G. Schnakenburg, K. Rissanen and A. Lützen, *Inorg. Chem.*, 2018, **57**, 3507-3515.
23. N. F. Chilton, R. P. Anderson, L. D. Turner, A. Soncini and K. S. Murray, *J. Comp. Chem.*, 2013, **34**, 1164-1175.